UNIVERSITY OF OKLAHOMA

GRADUATE COLLEGE

SEISMIC-CONSTRAINED LITHOLOGY PREDICTION AND RESERVOIR-QUALITY MODELING USING PRE-STACK INVERSION AND BAYESIAN CLASSIFICATION, MISSISSIPPIAN MERAMEC STRATA, EASTERN ANADARKO BASIN, OKLAHOMA

A THESIS

SUBMITTED TO THE GRADUATE FACULTY

in partial fulfillment of the requirements for the

Degree of

MASTER OF SCIENCE

By

MADISON HOPE WILLIAMS

Norman, Oklahoma

2020

SEISMIC-CONSTRAINED LITHOLOGY PREDICTION AND RESERVOIR-QUALITY MODELING USING PRE-STACK INVERSION AND BAYESIAN CLASSIFICATION, MISSISSIPPIAN MERAMEC STRATA, EASTERN ANADARKO BASIN, OKLAHOMA

A THESIS APPROVED FOR THE

SCHOOL OF GEOSCIENCES

BY THE COMMITTEE CONSISTING OF

Dr. Matthew Pranter, Chair

Dr. Kurt Marfurt

Dr. Deepak Devegowda

ACKNOWLEDGEMENTS

This research was made possible through the funding provided by Marathon Oil Corporation and the Reservoir Characterization and Modeling Laboratory at the University of Oklahoma (OU). I would like to recognize Marathon Oil, Oklahoma Petroleum Information Center (OPIC), and TGS for providing data. I thank Dr. Kurt Marfurt, Dr. Deepak Devegowda, Dr. Carl Sondergeld, and Dr. Chandra Rai for their leadership, feedback, and support throughout this project. I would like to thank Dr. Ali Tinni, Dick Larese, Ishank Gupta, Heyleem Han, Son Dang, and Jing Fu for providing numerous data measurements incorporated in this project. I would also like to acknowledge Micaela Langevin for all of her support and communication between Marathon Oil Corporation, the Reservoir Characterization and Modeling Laboratory, and the Integrated Core Characterization Center. Finally, I would like to acknowledge Schlumberger (Petrel), CGG (HampsonRussell), and the OU Attribute Assisted Seismic Processing and Interpretation (AASPI) Consortium for software.

I am extremely grateful to Dr. Pranter for providing me the opportunity to do this research, and for all of the guidance, advice, and encouragement throughout this journey. I would like to thank the RCML group, both past and present, as well as all of the friends I have made during my time here at OU for their continued support and companionship. I would like to thank my parents and my family including my three brothers Michael, Marshall, and Travis for their love and support. Above all, I would like to thank God for providing me with this amazing opportunity. I am very thankful for the knowledge, friendships, and memories that I have made during the duration of my Master's program.

TABLE OF CONTENTS

ABSTRACT

The Mississippian Meramec strata within the STACK (Sooner Trend in the Anadarko [Basin] in Canadian and Kingfisher counties) play of central Oklahoma is primarily a fine-grained mixed siliciclastic-carbonate system composed of mudstones, argillaceous siltstones, argillaceous-calcareous siltstones, and silty limestones. The Meramec interval within the study area ranges in thickness from 300 – 400 ft (91 – 122 m) and stratigraphically consists of seven parasequences, Meramec 1-7. The Meramec dips structurally to the southwest and is offset by several faults with varying throw that ranges from 50 to 150 ft (15 – 46 m). Five lithologies and three petrophysics-based rock types are classified in non-cored wells using a supervised Artificial Neural Network (ANN) based on well-log and core data. Elastic seismic attributes are derived from a pre-stack inversion to produce P-impedance, S-impedance, and density volumes. Elastic properties, P-impedance and S-impedance, are used to create lithology probability volumes for each lithology and a single lithology classification volume. Three-dimensional lithology and rock-type models illustrate the spatial distribution of stacked parasequences grading upward from argillaceous siltstone to calcareous siltstone. Petrophysical (porosity and water saturation) and geomechanical (Poisson's Ratio and Young's Modulus) property models show that lower values of porosity and higher value of water saturation are associated with brittle, calcareous-rich lithologies and rock types, and higher values of porosity and lower values of water saturation are associated with ductile, argillaceous-rich lithologies and rock types.

Comparisons to oil production suggest that higher reservoir productivity is associated with the mixed argillaceous and calcareous-rich rock type 2 and relatively more brittle rocks. The distribution of optimal reservoir quality parameters including geomechanical and petrophysical properties are associated with the stratigraphically controlled stacking pattern and

distribution of lithologies and rock types. Meramec parasequences 3 and 4, at the turnaround from retrogradational to progradational units, have the combination of depositional, petrophysical, and geomechanical characteristics associated with better reservoir quality and favorable drilling and hydraulic fracturing conditions.

INTRODUCTION

The Mississippian Meramec strata within the STACK (Sooner Trend of the Anadarko [Basin] in Canadian and Kingfisher counties) play of the eastern Anadarko Basin consists of deposits that represent a mixed carbonate-siliciclastic system. The Meramec of the STACK trend is, in part, the basinward equivalent of the carbonate and chert-rich Mississippian deposits of northern Oklahoma and southern Kansas, informally known as the "Mississippi Lime". Unlike the Meramec, the "Mississippi Lime" reservoirs of the highly porous, weathered, and chert-replaced Mississippian section (Watney et al., 2001) have been the focus of extensive studies revealing the depositional history and spatial variability of the Mississippian limestone in north-central Oklahoma, as well as the depositional and diagenetic controls on reservoir properties (e.g., Peeler, 1985; Parham and Northcutt, 1993; Montgomery et al., 1998; Rogers, 2001; Watney, 2001; Mazzullo, 2011; Grammer et al., 2013; Cahill, 2014; LeBlanc, 2014; Doll, 2015; Mazzullo et al., 2016; Drummond, 2018; Price and Grammer, 2018; Wethington and Pranter, 2018; Lindzey et al., 2019; Turnini et al., 2019). A shift in depositional style is observed within the Mississippian strata from northern to central Oklahoma as the shallow-water carbonate system of northern Oklahoma transitions to a mixed carbonate and siliciclastic system of primarily siltstones and mudstones (Curtis and Champlin, 1959; Watney et al., 2001; Price et al., 2017; Drummond, 2018; Duarte; 2018; Hardwick, 2018; Hickman, 2018; Miller, 2019; Miller et al., 2019; Hardisty, 2019; Price et al., 2020) (Figure 1).

Relative changes in sea level is suggested to impart a strong control on reservoir quality as the stacked shallowing-upward parasequences transition upward from those that exhibit more argillaceous siltstones to parasequences with more calcareous siltstones (Drummond, 2018; Duarte, 2018; Price et al. 2017; Miller, 2019; Miller et al., 2019; Hardisty 2019; Price et al.,

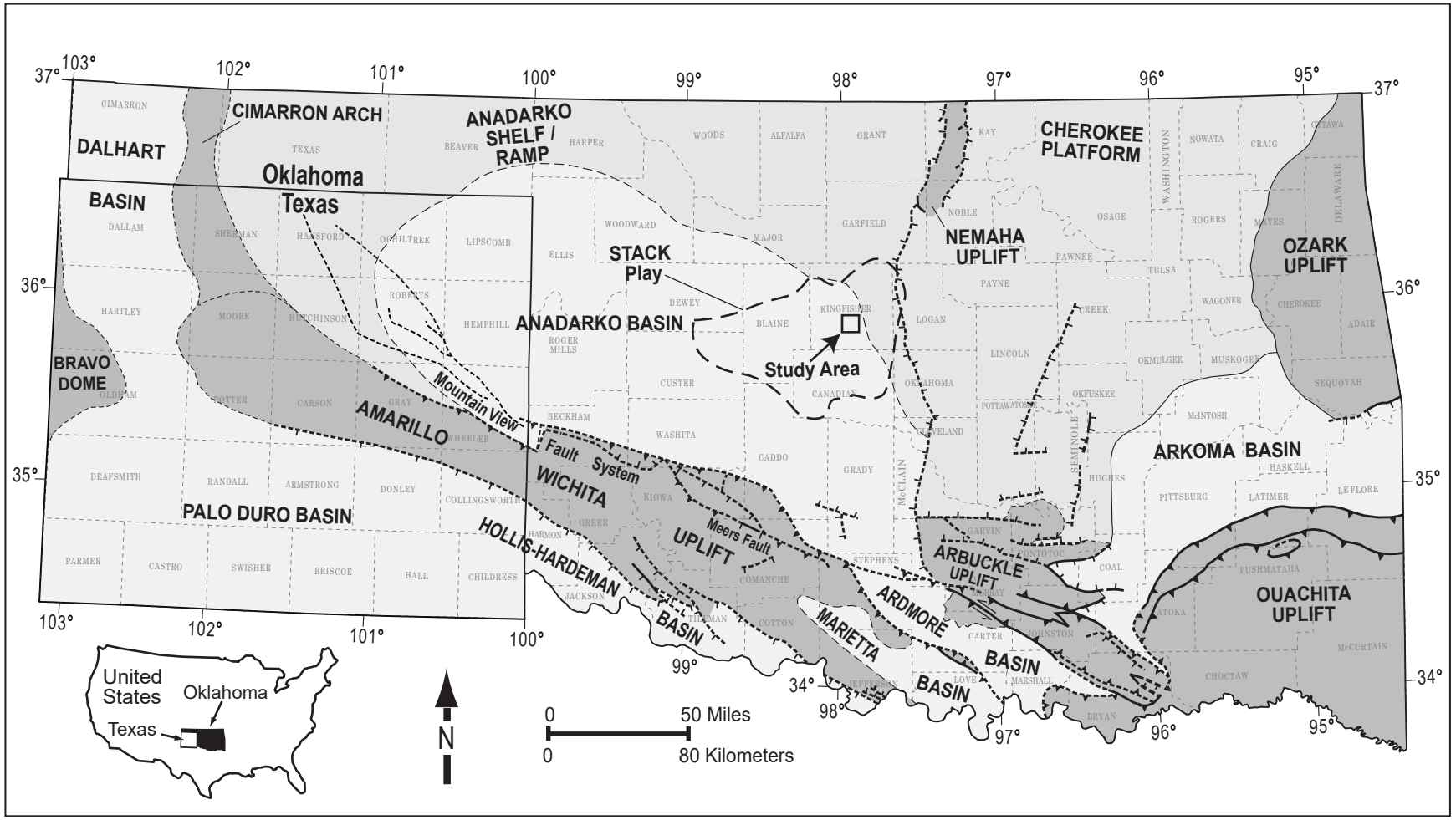

Figure 1: Regional tectonic map of Oklahoma and the Texas panhandle. The study area is outlined within the STACK play of the eastern Anadarko Basin (Dutton, 1984; Campbell et al., 1988; McConnell, 1989; Northcutt and Campbell, 1995; Johnson and Luza, 2008; LoCriccho, 2012).

2020). Hardwick (2018), Miller (2019), and Price et al. (2020) find the quantity of calcite cement is considered to be a primary driver of reservoir quality in the Meramec, as more clay content inhibits calcite cementation and preserves some primary porosity.

Drummond (2018) integrated core and well-log data to interpret shallowing-upward depositional cycles and establish a regional stratigraphic framework of the Mississippian. Drummond (2018) incorporated machine learning and 3D reservoir modeling to illustrate the spatial distribution of Meramec lithologies and petrophysical properties.

There are few studies concerning seismic characterization of the Meramec in the eastern Anadarko Basin. Within the Mississippian limestone, Dowdell et al. (2013) combined pre-stack seismic inversion attributes with geometric attributes and horizontal image logs to identify sweet spots comprised of high porosity and high fracture density. Lindzey et al. (2019) and Turnini et al. (2019) demonstrated the spatial distribution of key lithologies and petrophysical properties within the Mississippian limestone through seismic-constrained 3D reservoir modeling techniques. Both Lindzey et al. (2019) and Turnini et al. (2019) observed that anomalously low impedance values indicated tripolitic chert within the reservoir and therefore used the impedance data as a constraint in the 3D reservoir modeling. Relationships between key reservoir properties and the production success of wells drilled in the areas were also analyzed in their studies (Lindzey et al., 2019; Turnini et al., 2019).

This study further investigates the variability of key lithologies, rock types, and petrophysical and geomechanical properties of the Mississippian strata within the STACK trend. Specifically, this study addresses the following questions:

1. What is the seismic expression of stratigraphic (parasequences) and structural features?

2. What is the spatial variability of lithologies, rock types, petrophysical properties, and geomechanical properties?
3. How do petrophysical and geomechanical properties relate to lithologies, rock types, stratigraphy, and reservoir performance?

The study area is within Kingfisher County, Oklahoma (Figure 2). Data include a 36 mi^2 (58 km^2) 3D post-stack time-migrated seismic volume, time-migrated conditioned pre-stack seismic angle gathers, 86 wells (include logs for 44 vertical and 42 horizontal wells), core descriptions, x-ray diffraction (XRD) data, x-ray fluorescence (XRF) data, and thin-section photomicrographs. This study uses core information (Well A, the Gulf Oil Corp 1-23 Shaffer, and the Gulf Oil Corp 1-25 Rohling) and well-log and 3D seismic data to interpret the stratigraphic and structural framework of the areas. Well A is located outside of the model boundary. A pre-stack seismic inversion using conditioned angle gathers yielded P-impedance, S-impedance, and density attributes. The seismic attributes were used as a constraint to model lithologies, rock types, and petrophysical and geomechanical properties. The relationships between reservoir properties and production is also examined.

GEOLOGIC SETTING

The Anadarko Basin is a northwest trending, asymmetrical foreland basin covering western Oklahoma, northern Texas Panhandle, southern Kansas, and southwestern Colorado (Beebe, 1959). The basin is bounded to the east by the Nemaha uplift, the Arbuckle uplift and Ardmore Basin to the southeast, the Wichita-Amarillo uplift to the south, and the Hugoton Embayment to the northwest. The basin shallows northward and grades into a broad shelf onto the Central Kansas uplift (Perry, 1990; Ball et al., 1991; Gallardo and Blackwell, 1999). The

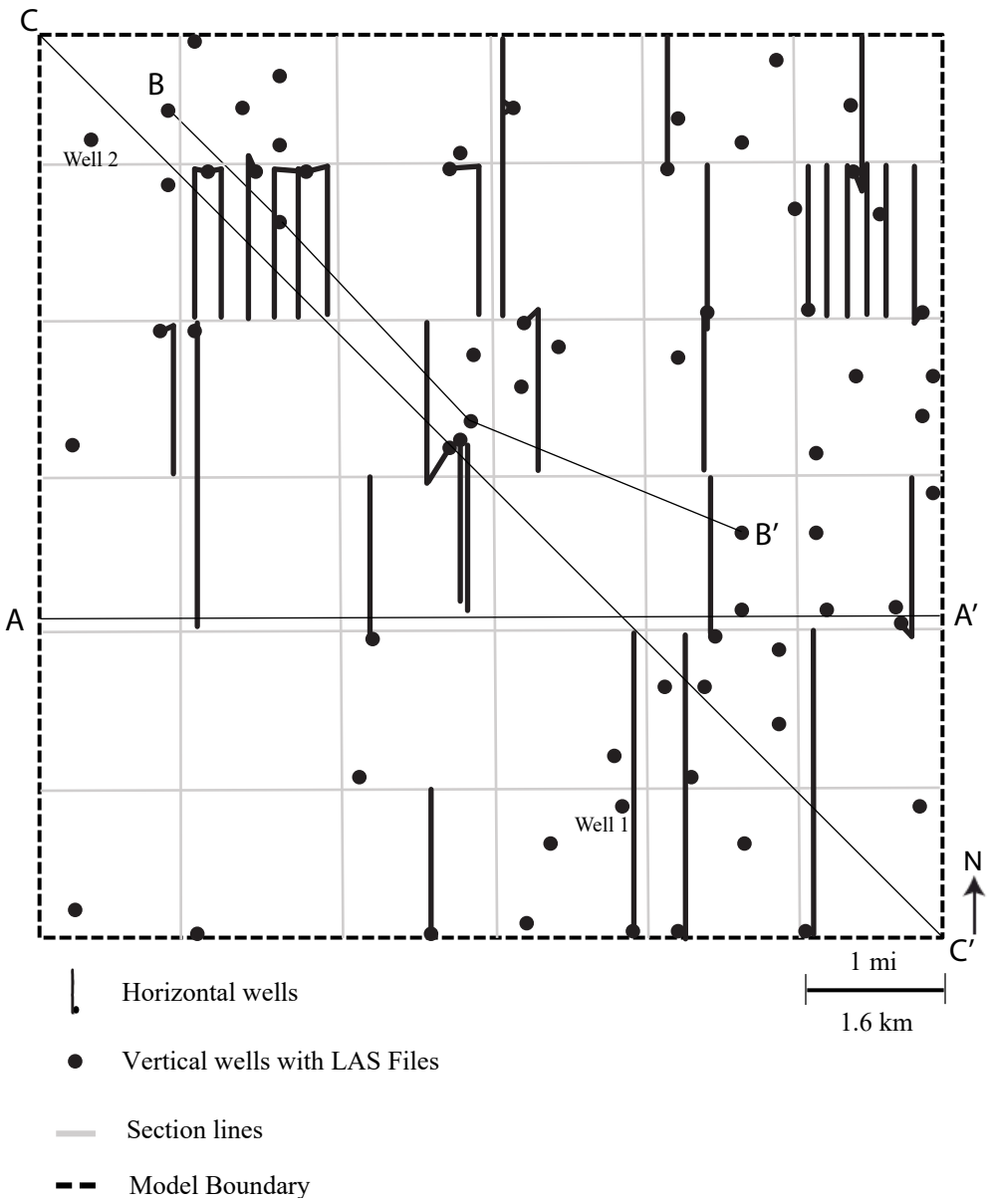

Figure 2: Map of study area showing well locations and well-log cross sections and seismic sections of interest. The study area is covered by a 3D seismic survey and also corresponds to the 3D reservoir model area. The data also include 86 wells (44 vertical wells with digital well-log data and 42 horizontal wells). Seismic section A-A' is shown as Figure 4. Well-log and model cross section B-B' is shown as Figure 9. Model cross sections for C-C' are shown as Figures 12, 14, and 15. Map location is shown on Figure 1.

Anadarko Basin contains more than 40,000 ft (12,000 m) of Cambrian through Permian sediments at its deepest point along the southern margin at the edge of the Wichita Mountains uplift (Ham and Wilson, 1967).

The paleolatitude of the study area during the Mississippian is between 20º-30º S, placing it in a tropical to subtropical environment (Appendix-A1) (Curtis and Champlin, 1959; Witzke, 1990; Mazzulo et al., 2016). A warm, shallow sea covered the North American craton during this time, depositing Mississippian sediments throughout the continent. Sediments deposited within the Anadarko Basin occurred on a low-relief ramp and are described as a system of low inclination (less than 1º) deep-water prograding clinoforms with strike-elongate in a northeast-southwest orientation and progradation of the clinoforms to the southeast along the ramp (Curtis and Champlin, 1959). The Mississippian deposits represent an interval of transition from Early Paleozoic greenhouse conditions with lower amplitude sea-level changes to Late Paleozoic icehouse conditions with higher amplitude sea-level fluctuations (Read, 1995; Haq and Schutter, 2008).

The Mississippian interval represents a single 2nd-order transgressive-regressive cycle bounded by a basal disconformity (Comer, 1991) and an overlying unconformity associated with the Kaskaskia Sequence (Sloss, 1963). It also includes several higher order transgressive-regressive cycles. In this part of the mid-continent, the Mississippian Period is divided into four series, in ascending order, Kinderhookian, Osagean, Meramecian, and Chesterian (Curtis and Champlin, 1959; Northcutt et al., 2001). The lithologies within the Meramecian strata in the study area have been defined by several previous studies as primarily mudstones, calcareous to argilliaceous siltstones and some very fine sandstones (Drummond, 2018; Duarte, 2018; Hickman, 2018; Miller, 2019; Miller et al., 2019; Price et al., 2020).

METHODS

Lithology and Rock-Type Definition and Classification

Mississippian Meramec lithologies include mudstones, argillaceous siltstones, argillaceous-calcareous siltstones, calcareous siltstones, and silty limestones as defined in the study area by Miller (2019) (Table 1; Figure 3). Miller (2019) defined lithologies by integrating detailed core descriptions with petrographic data, and calculated mineralogy from X-ray fluorescence data (Han et al., 2019). This information was derived from three cored wells near the study area: Well A (core length = 485 ft [148 m]), the Gulf Oil Corp 1-23 Shaffer (242 ft [74 m]), and the Gulf Oil Corp 1-25 Rohling (207 ft [63 m]) (Miller, 2019). Gupta (2018, personal communication) petrophysically defined three rock types based on cross plots of core-measured permeability (air) and porosity, and applied Flow Zone Indicator (FZI) cutoffs to the data (Appendix-B1). To calculate the FZI cutoff, the ratio of the Reservoir Quality Index (RQI) and the pore-to-grain volume (R_{pvgv}) is defined by the following equations (Amafule et el., 1993):

$$RQI = 0.0314 * \sqrt{\frac{k}{\emptyset}}, \quad (1)$$

$$R_{pvgv} = \frac{\emptyset}{1 - \emptyset}, \text{and} \quad (2)$$

$$FZI = \frac{RQI}{R_{pvgv}}, \quad (3)$$

where:

k = permeability,

ø = porosity,

R_{pvgv} = pore-to-grain volume ratio,

RQI = Reservoir Quality Index, and

FZI = Flow Zone Indicator.

Lithology	Lithofacies	Description	Depositional Setting
Mudstone	Structureless Mudstone	Clay minerals prominant with silt-sized quartz grains . Calcite cement along with sparse shell fragments.	Distal marine well below storm wave base
Argillaceous Siltstone	Silty Laminated Mudstone	Clay minerals prominant with silt-sized quartz grains and some calcite and quartz cement. Faint planar laminations.	Offshore marine (outer ramp) at or below storm wave base
	Silty Bioturbated Mudstone	Clay minerals present with silt-sized quartz grains and some calcite and quartz cement. Bioturbation destroyed sedimentary structures.	Outer to mid-ramp at or below storm wave base (Transition Zone)
Argillaceous Calcareous Siltstone	Calcareous Bioturbated Siltstone	Clay minerals and calcite/quartz cement matrix with detrital silt-sized quartz grains. Heavily bioturbated, with fossil fragments.	Outer to mid-ramp within fair weather wave base (Transition Zone)
	Calcareous Laminated Siltstone	More calcite/quartz cement than clay minerals in matrix with silt-sized quartz grains. Faint to visible planar laminations.	Mid-ramp within fair weather wave base
Calcareous Siltstone	Structureless, Calcareous Sandstone/Siltstone	Very-coarse silt to very-fine sand sized quartz grains. Abundant calcite/quartz cement. Calcite cemented fractures.	Mid-ramp within fair weather wave base (Turbidite event)
	Cross-Stratified, Calcareous Sandstone/ Siltstone	Very-coarse silt to very-fine sand sized quartz grains. Abundant calcite/quartz cement. Planar to curved laminations.	Mid-ramp within fair weather wave base (Turbidite/storm events)
Silty Limestone	Skeletal Silty Packstone to Grainstone	Abundant peloids and skeletal grains with some silt-sized quarts grains. Prevalent calcite cement.	Lower shoreface (inner ramp) within fair weather wave base (shoals)

Table 1: Summary of the Meramec lithologies in the study area (Miller, 2019).

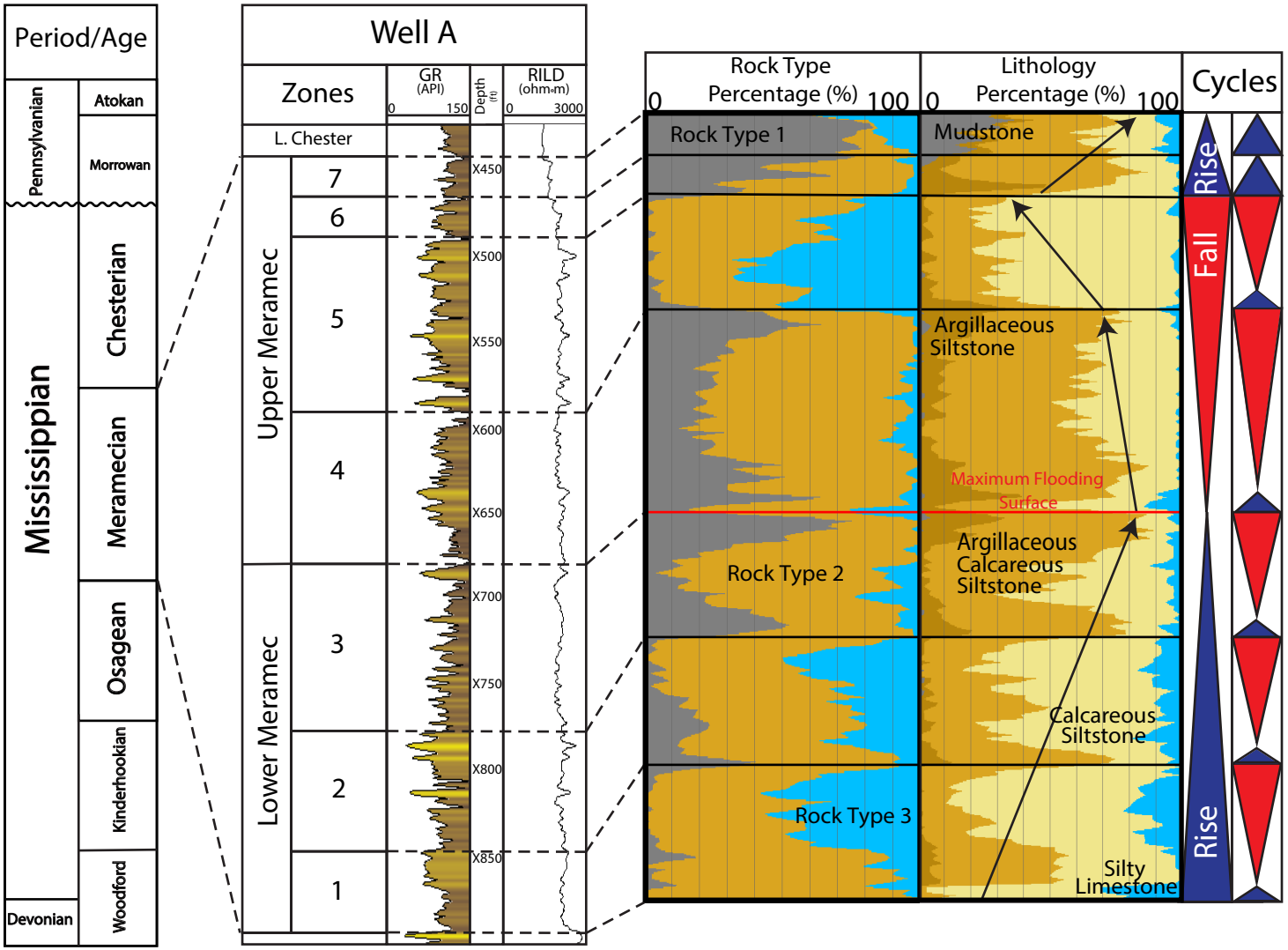

Figure 3: Generalized Mississippian section stratigraphic column to the left (Modified from Boyd, 2008) correlating to a type log with the interpreted internal zones of the Mississippian Meramec. The type log is tied to the rock-type and lithology vertical proportion curves on the right. The vertical proportion curves illustrate the stratigraphic variability of rock types and lithologies in the study area. Stratigraphic cycles are shown (Modified from Miller, 2019).

Miller (2019) also classified lithologies and rock types in non-cored wells through electrofacies classification utilizing supervised Artificial Neural Networks [ANN]. Electrofacies classification is a method that is used to describe a rock in terms of its well-log characteristics (Serra and Abbott, 1982). This approach establishes a relationship between well-log values and the lithologies and rock types in the study by comparing the well-log signature to its corresponding cored lithology or rock-type interval. Miller (2019) used a supervised Artificial Neural Network [ANN] and a log suite consisting gamma ray (GR), neutron porosity (NPHI), bulk density (RhoB), and photoelectric effect (PE) to classify lithologies and rock types for Well A. The established relationships between the lithologies and rock types and the well-log responses were applied to non-cored wells, thereby providing an estimate of lithology and rock type for all vertical wells in the study area.

Stratigraphic and Structural Framework

The Meramec stratigraphy was interpreted initially using 44 vertical wells within the study area using the estimated lithology logs, conventional well logs (gamma-ray, neutron porosity, density porosity, bulk density, and resistivity), and a grid of dip- and strike- oriented well-log cross sections.

The formation tops were used as a guide to interpret corresponding horizons in the seismic volume. The formation well tops that align with a distinct peak, trough, or zero-crossing in the seismic data were picked as horizons. The cosine of phase seismic attribute was applied to the volume to aid in the interpretation of discontinuous reflectors. This attribute allows reflection continuity to be easier to recognize by acting “like a perfect automatic gain control (AGC) in that it removes all amplitude information” (Barnes, 2007). Based on the seismic data resolution, the top, base, and one internal parasequence of the Meramec were interpreted on the seismic volume.

The remaining seismic-constrained horizons that represent thinner stratigraphic intervals were established using a conformable gridding algorithm that incorporates the upper and lower interpreted seismic horizons and the associated well tops. This operation conformably generates seismic-guided horizons for all zones within the Meramec. Structure-contour and isopach maps were constructed to check the quality of the interpretations and to analyze Meramec stratigraphic trends.

Major faults were interpreted for the study area using structure-contour maps, seismic multi-attribute structural interpretations, and well-log cross sections. Structure-contour maps distinguish areas with sharp dip changes which could be indicative of faults. Structural seismic interpretation includes identifying and mapping faults distinguished by: (1) amplitude offsets in the seismic vertical-cross sections and time slices and (2) linear, incoherent features highlighted by the geometric attribute, coherency. Seismic coherency marks discontinuities where there are lateral changes in the trace-to-trace seismic response. Utilizing the coherency and amplitude data, faults were interpreted in vertical seismic sections and time slices. Faults were interpreted initially in areas with the greatest reflector offset and extended upward or downward until the reflectors were more continuous. Only faults extending through the Mississippian Meramec formation are interpreted (Figure 4). The amount of throw along each of the faults was quantified by measuring vertical offset seen on the amplitude data volume, while accounting for formation dip.

Pre-stack Seismic Inversion

A pre-stack seismic inversion is conducted to obtain reliable estimates of P-impedance, S-impedance, and density. Before executing the pre-stack seismic inversion, a post-stack inversion was performed using the horizons, wells with bulk density and sonic logs, and the

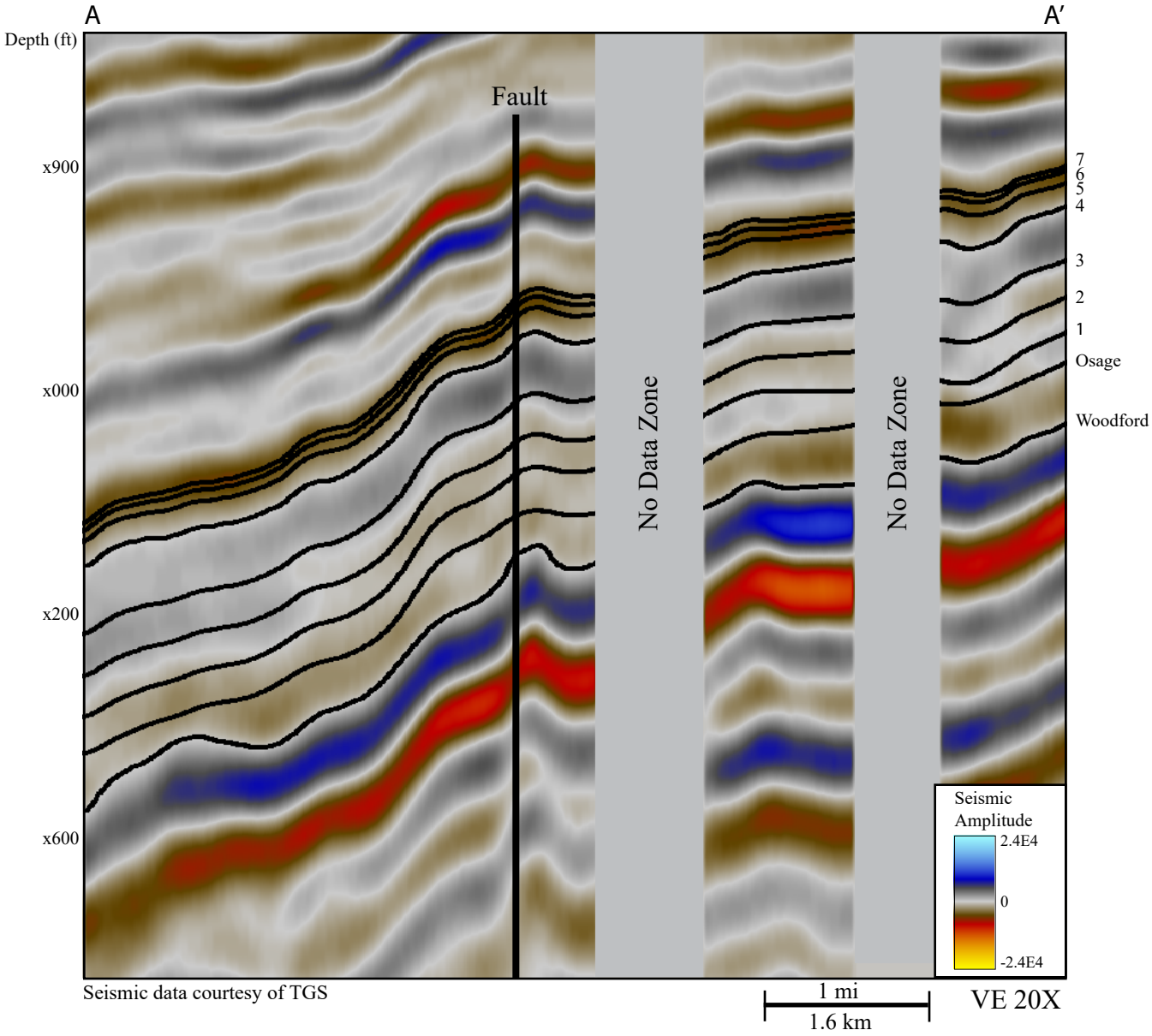

Figure 4: Seismic section A-A' showing the seismic amplitude with the interpreted Meramec parasequences 1-7, Osage, and Woodford horizons bisecting a north-south oriented fault. The top Meramec, top parasequence 4, and base Meramec were interpreted on the seismic volume, and the other stratigraphic horizons were mapped using conformable gridding with the associated well tops. Location of seismic section is shown on Figure 2.

stacked seismic volume to produce a P-impedance volume. A pre-stack seismic inversion was performed to investigate the spatial distribution of rock properties, and to use as a constraint in 3D lithology, rock-type, and petrophysical property models. The steps to perform the pre-stack inversion include: (1) data organization, (2) wavelet extraction and seismic-to-well tie, (3) low-frequency background model generation, and (4) pre-stack seismic inversion execution (Figure 5).

The pre-stack seismic inversion inputs include the seismic horizons (top of Meramec 7, Meramec 3 [maximum flooding surface], Osage, and Woodford), 25 vertical wells with synthetic compressional sonic (DTC), synthetic shear sonic (DTS), and density (RhoB) logs, and seismic-angle gathers. Synthetic sonic logs were generated using a multi-variable analysis (C. McLain, 2019, personal communication). Seismic gather traces correspond to angle of incidence, ɵ, for reflected energy as related to offset, X (Appendix-C1). If the angle of incidence is greater than zero, there is both a compressional and shear component (Russell, 2014). The seismic angle gathers include incident angles up to 60º. However, to reduce the additive noise that the far angles introduce, an angle mute was performed for incident angles greater than 45º.

Well ties to seismic data were performed on 25 wells using commercial software by first estimating a statistical angle-dependent wavelet group consisting of three angles for low (4°-17°), mid (17°-31°), and far (31°-45°) angles from the seismic angle gathers (Figure 6). Reflection coefficients calculated from the compressional sonic (DTC), shear sonic (DTS), and density (RhoB) logs are convolved with the low-angle (4°-17°) statistical wavelet producing a synthetic seismogram. The synthetic seismogram was modified by bulk shifts and minor stretch and squeeze edits to match the synthetic seismogram with the original time-migrated seismic trace.

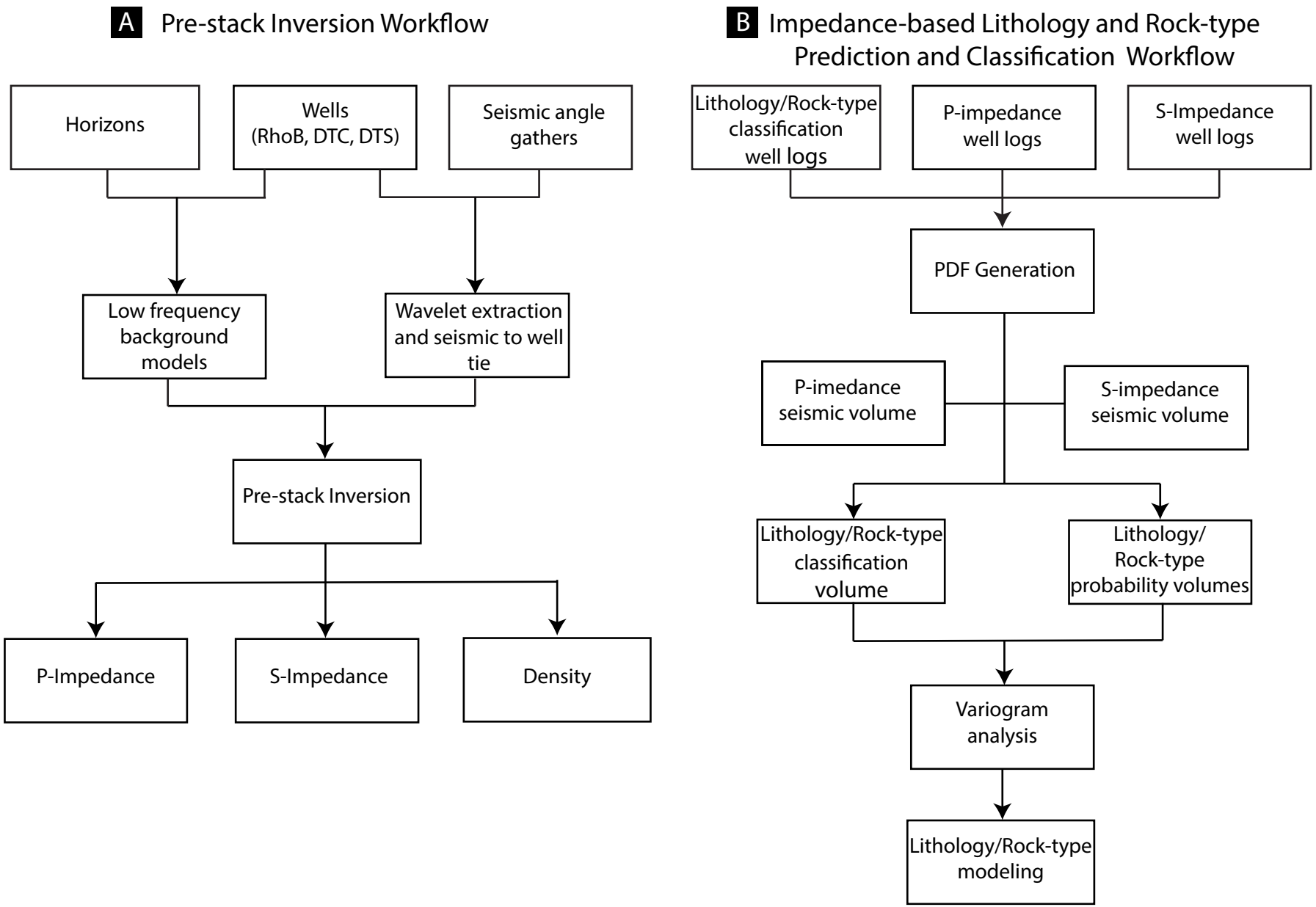
A Pre-stack Inversion Workflow
Horizons
Wells (RhoB, DTC, DTS)
Seismic angle gathers
Low frequency background models
Wavelet extraction and seismic to well tie
Pre-stack Inversion
P-Impedance
S-Impedance
Density
B Impedance-based Lithology and Rock-type Prediction and Classification Workflow
Lithology/Rock-type classification well logs
P-impedance well logs
S-Impedance well logs
PDF Generation
P-imedance seismic volume
S-impedance seismic volume
Lithology/Rock-type classification volume
Lithology/ Rock-type probability volumes
Variogram analysis
Lithology/Rock-type modeling

Figure 5: A) Generalized pre-stack inversion workflow. The seismic horizons and wells (DTC, DTS, and RhoB) were used to build the low frequency background models. The wells and the seismic angle gathers were used for the wavelet extraction and the seismic-to-well ties. The horizons, models, wavelets, and seismic angle gathers were then used to perform a pre-stack inversion producing P-impedance, S-impedance, and density volumes. B) Generalized workflow of the impedance-based lithology and rock-type prediction and classification process. The first step involves using the lithology, rock-type, p-impedance, and s-impedance well logs to relate lithologies and rock types to p- and s-impedance. This relationship defines probability density functions (PDFs) for each lithology and rock type. The PDFs are utilized with the p-impedance and s-impedance seismic volumes to generate a lithology and rock-type classification volume and probability volumes for each lithology and rock type. These volumes are used in variogram analysis and to constrain 3-D reservoir modeling to produce 3-D seismic-constrained lithology and rock-type models.

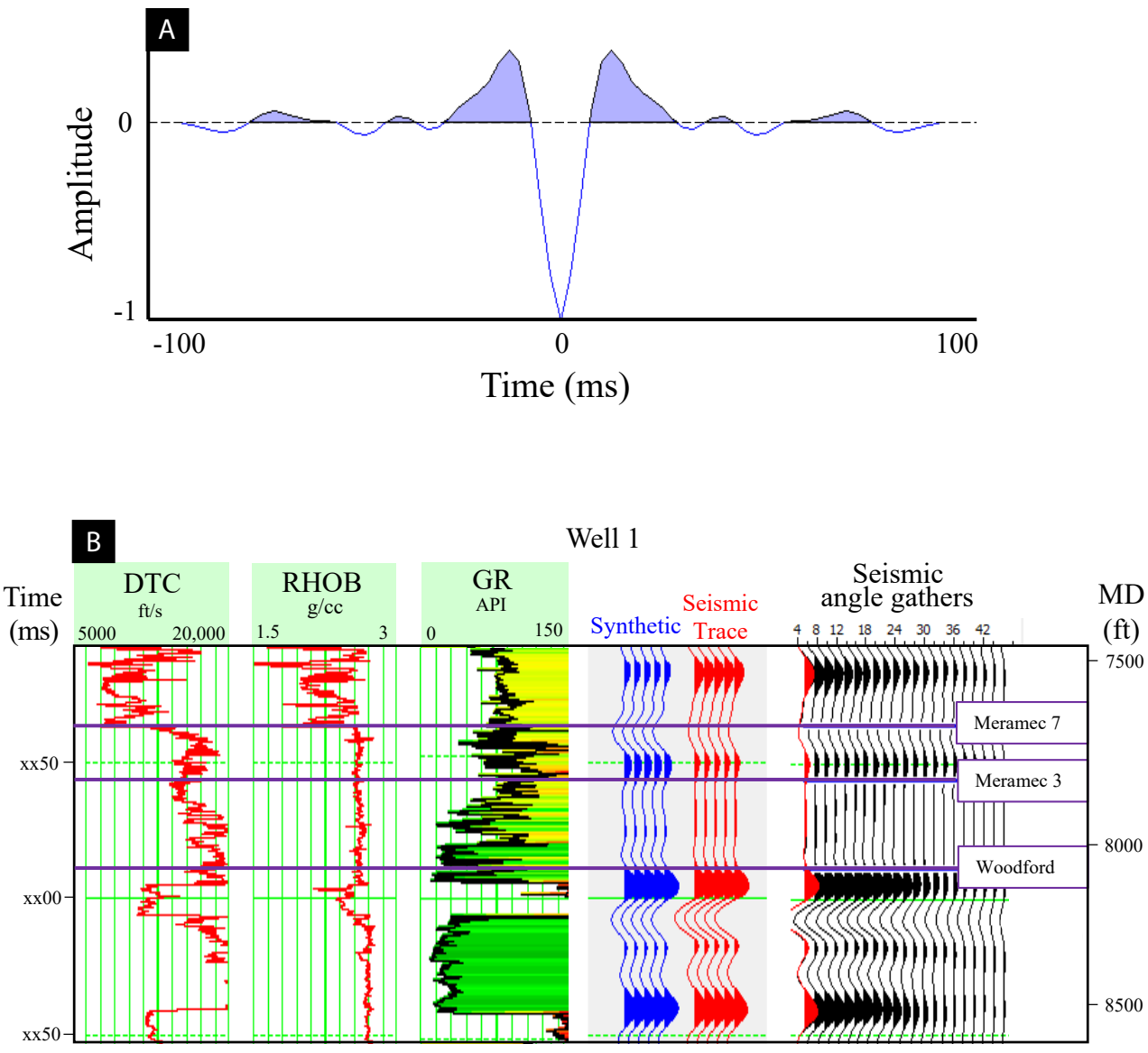

Figure 6: A) The extracted statistical angle dependent wavelet for the low (4º-17º) angles and B) the seismic-to-well tie for Well 1. The synthetic seismogram generated from the low angle wavelet, and the sonic and density logs were adjusted to match the original seismic trace at the well location resulting in a cross-correlation of 84%.

Low-frequency background models are required for inverting the angle gathers simultaneously for multiple properties. The low-frequency background models use the well data to compensate for the absent low frequency part of the seismic spectrum because well-log measurements of elastic properties contain a full range of frequencies from zero to well above the highest seismic frequencies (Sams and Carter, 2017). The seismic amplitude spectrum of the angle gathers shows that the amplitude rolls off to zero from 10 Hz to 5 Hz; therefore, the low-frequency background models were developed using well logs with a high-frequency cutoff range of 5-10 Hz. The high-cut frequency logs of P-impedance, S-impedance, p-wave velocity, s-wave velocity, and density values were interpolated using Kriging within the stratigraphic framework to generate 3D low-frequency background models for the pre-stack inversion.

The pre-stack seismic angle gathers provide information about the elastic properties of the seismic by describing reflectivity as a function of angle (Appendix-C2). Seismic inversion allows for the distribution of these measured properties from wells throughout the seismic volume. In principle, a pre-stack seismic inversion is the reverse process to the forward modeling of acoustic impedance reflectivity convolved with a wavelet resulting in a seismic trace. Although a complete reversal is never achieved as the band-limited seismic data is contaminated with noise resulting in approximations of the properties. A model-based simultaneous inversion was executed using commercial software by first computing a synthetic offset seismic from the initial impedance model. The difference between the synthetic and the real seismic data is determined and iteratively updated using the conjugate gradient method until the derived synthetic seismic data best fits the observed seismic data, or a global minimum is achieved (Hampson et al., 2006). The simultaneous inversion examines all traces to invert for a globally constrained optimization model (Barclay et al., 2008) to produce estimates of P-impedance, S-

impedance, and density. Three key assumptions are made in the algorithm used for this study: 1) the linearized approximation for reflectivity holds, 2) reflectivity as a function of angle can be approximated by the Aki-Richards equations, and 3) there is a linear relationship between the logarithm of P-impedance and both S-impedance and density (Hampson et al., 2006). Several quality control steps were executed to ensure that the results of the inversion are accurate representations of the elastic properties from the seismic and well-log data.

The results of the pre-stack seismic inversion contain additional information about the rock properties of the reservoir and are used to generate the geomechanical properties: Poisson's Ratio (ν) and Young's Modulus (E) (Appendix-C3).

Velocity Modeling

The pre-stack inversion results (P-impedance, S-impedance, density, Poisson's Ratio, and Young's Modulus volumes) were converted from the time to depth domain. This was achieved by building a velocity model using instantaneous velocities from the wells with time-depth relationships (TDR) from the seismic-to-well ties and the seismic time horizons (from base to top): Woodford Shale, Meramec 3 (maximum flooding surface), and Meramec 7. Instantaneous velocity is modeled with depth using a linear equation so that the model layer velocities vary with depth and by stratigraphic zone (Etris et al., 2002) (Appendix-D1).

Impedance-Based Lithology and Rock-Type Prediction and Classification

Impedance-based lithology and rock-type prediction is a rock physics-based process that was performed to estimate the most probable lithology or rock type, with prediction uncertainty, as they relate to P-impedance and S-impedance (Figure 5). Inputs include the lithology and rock-type logs, P-impedance and S-impedance logs, associated seismic inversion volumes, well-based formation tops, and seismic-depth surfaces. A Bayesian approach involving a Monte Carlo

simulation allows for the assemblage of initial, or prior, knowledge about a model before the incorporation of seismic attributes (Bachrach et al., 2004) which is defined in this study by the percentages of each lithology or rock type within the formation. The prior knowledge is incorporated in the simulation to determine the relationships between lithologies and rock types and elastic well-log properties (P-impedance and S-impedance) resulting in the associated statistical probability density functions (PDFs). P-impedance and S-impedance logs are chosen as input because P-impedance provides information about the porosity and hydrocarbon presence within the rock and S-impedance gives clues regarding the lithology without the effects of pore space and fluid. The P-impedance is calculated from the density and synthetic compressional sonic logs (DTC), and the S-impedance log is calculated using the following equation for s-wave velocity derived from core velocity measurements (J. Fu, S. Dang, and H. Han, 2019, personal communication):

$$V_s = 1.29 + 0.35 * V_p,$$

where:

V_s = s-wave velocity

V_p = p-wave velocity.

The results of the impedance-based lithology and rock-type predictions are used to generate lithology and rock-type probability volumes and one classification volume each for lithology and rock type (3D property volumes) by applying the statistical PDFs to the P-impedance and S-impedance seismic volumes. The most-likely lithology or rock type is chosen by using the maximum a priori rule (Kay, 1993) on the inversion data, as the different data at one point is collected into a sample vector where all PDFs for the different lithologies and rock types are evaluated and the PDF that is the largest for this vector is chosen as the predicted lithology or

rock type for that point (Bachrach et al., 2004). For the lithology model, the impedance-based lithology prediction workflow was performed separately for the Meramec interval above and interval below the maximum flooding surface due to differences in the percentages of lithologies for those intervals.

3D Reservoir Modeling

For the Meramec, lithology and rock-type models (30 realizations each) were generated to assess their variability and the associated variability of porosity, water saturation, pore volume, and hydrocarbon pore volume (HCPV). A faulted 3D reservoir model grid was generated by incorporating the stratigraphic surfaces (structure-contour maps) established from the interpreted formation seismic horizons, well tops, interpreted fault surfaces, and their associated vertical offsets (Figure 7). The 3D grid covers an area ~36 mi^2 (~60 km^2). The aerial cell dimensions correspond to the seismic bin size of 110 ft x 110 ft (33.5 m x 33.5 m) with an approximate layer thickness of 2 ft (0.6 m). The grid is comprised of 288 x 283 x 185 cells in the I, J, and K directions, respectively, resulting in 16,056,288 cells with a proportional layering scheme. The 3D model grid was generated as a representation of the structural and stratigraphic framework of the Meramec.

To constrain the spatial distribution of lithologies and rock-types, well logs and the lithology volumes derived from the impedance-based lithology prediction process were used to derive vertical and horizontal variograms, respectively, for each of the lithologies and rock types. Vertical variograms were created using the lithology and rock-type logs. The classification volumes representing the most-likely lithology or rock type were resampled to the 3D model grid and converted into corresponding discrete property models. The discretized lithology and rock-type models were then used to generate horizontal variograms for each property by zone. The

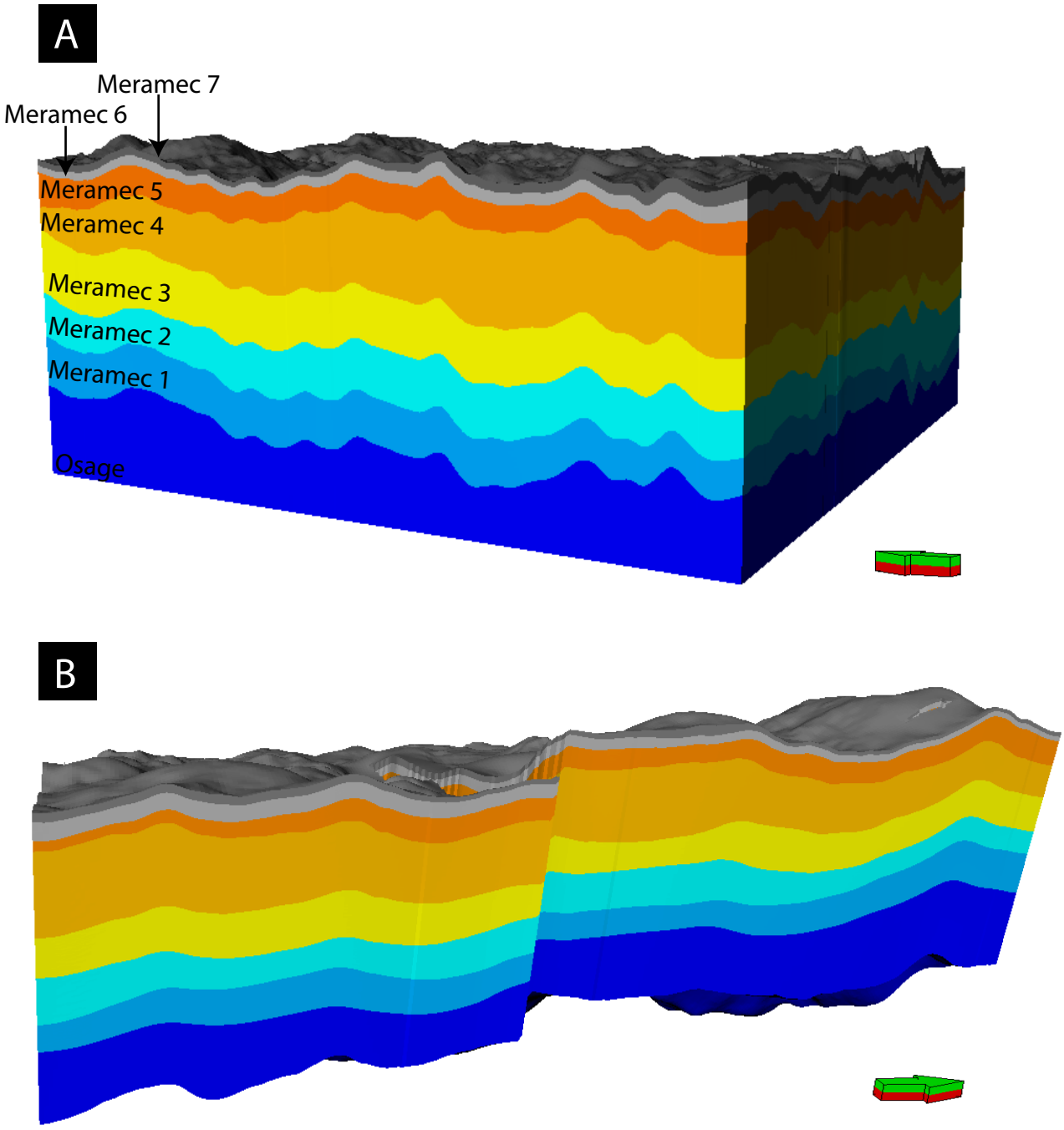

Figure 7: Three-dimensional model framework of the Mississippian Meramec formation overlaying the Osage formation. The 3-D grid covers an area ~36 mi2 (~60 km 2) with aerial cell dimensions corresponding to the seismic bin size of 110 ft x 110 ft (33.5 m x 33.5 m) with an approximate layer thickness of 2 ft (0.6 m). The grid is comprised of 288 x 283 x 185 cells in the I, J, and K directions, respectively, resulting in 16,056,288 cells with a proportional layering scheme. The top image A) is vertically exaggerated 25X showing Meramec parasequences 1-7 and flattened on the bottom horizon. B) shows the unflattened faulted 3-D model grid exaggerated 15X highlighting one of the 150 ft (46 m) faults. This model represents the structural and stratigraphic framework of the Meramec.

probability volumes for each facies were used to generate variogram maps to estimate the major and minor range azimuths. For total porosity and water saturation (S_w) modeling, the corresponding logs were used to determine the vertical variogram ranges, and appropriate horizontal variogram ranges were approximated for the major and minor directions.

3D lithology and rock-type models were generated using sequential-indicator simulation (SIS) to represent their spatial variability within the Meramec. The models are constrained by: 1) the stratigraphic and structural framework (faulted 3D grid), 2) upscaled lithology and rock-type logs, 3) variogram parameters by zone, 4) lithology and rock-type percentages by zone, and 5) seismic impedance-based lithology and rock-type probability volumes. The logs were upscaled to the 3D model grid by assigning a cell a single lithology or rock-type class based on the most abundant lithology or rock type within the cell. The lithology and rock-type percentages by zone were obtained from the upscaled logs.

Two 3D porosity models were generated to analyze the spatial distribution of total porosity (PHI_{Tot}). The lithology-based porosity model was generated using sequential-Gaussian simulation (SGS) with the following modeling constraints: 1) 3D lithology model, 2) upscaled PHI_{Tot} logs biased to the lithology logs using an arithmetic mean, 3) porosity histograms by zone and lithology, and 4) variogram parameters by zone and lithology. The rock type-based porosity model was similarly generated using SGS with the following modeling constraints: 1) 3D rock-type model, 2) upscaled PHI_{Tot} logs biased to the rock-type logs using an arithmetic mean, 3) porosity histograms by zone and rock type, and 4) variogram parameters by zone and rock type.

Two 3D water saturation (S_w) models were generated to evaluate the spatial distribution of water saturation. Miller (2019) calculated the S_w logs using the basic Archie equation with parameters derived from core and lab measurements (Ali Tinni, 2019, personal communication),

resistivity logs, and PHI_{Tot} logs. The lithology-based S_w model was generated using SGS and constrained to: 1) the 3D lithology model, 2) upscaled S_w logs (biased to lithology), S_w histograms by zone and lithology, and variogram parameters by zone and lithology. Additionally, the rock type-based S_w model was generated using SGS and constrained to: 1) the 3D rock type model, 2) upscaled S_w logs (biased to rock type), S_w histograms by zone and rock type, and variogram parameters by zone and rock type.

Geomechanical property models, Poisson's Ratio (*v*) and Young's Modulus (*E*), were generated directly by resampling the depth-converted, inversion-derived Poisson's Ratio and Young's Modulus volumes to the 3D grid. The distribution of *v* and E values throughout the Meramec in the study area was evaluated, and relative cutoffs were applied to both properties discretizing them into ductile, intermediate, and brittle facies. For Poisson's Ratio (*v*), distinct cutoffs generated the following three properties: 1) high *v* (ductile), 2) intermediate *v*, and 3.) low *v* (brittle). Poisson's Ratio is associated with the strength of a rock. Hence, the low values of *v* indicate rocks that would be easier to break and vice versa. The high *v* rocks include all values of Poisson's Ratio >0.27, and the low *v* group includes all values <=0.23. For Young's Modulus (E), the discretized properties include: 1) low *E* (ductile), 2) intermediate *E*, and 3) high *E* (brittle). Considering Young's Modulus is a measure of the stiffness of a rock low values are associated with easily conformable, ductile material. The low *E* rocks include all values of Young's Modulus <40, and the high *E* facies encompasses all values >= to 52. Geomechanical facies proportion maps per zone were generated to compare the percentages of the geomechanical *v* and *E* rocks within each of the Meramec zones.

Volumetrics

To assess the range of uncertainty associated with the pore volume and hydrocarbon pore volume (HCPV) of the 3D lithology and rock-type models, multiple realizations are executed, and the range of values evaluated. The volumetric uncertainty analysis was performed for the lithology- and rock-type-constrained PHI_{Tot} and S_w models by generating 30 realizations of pore volume and HCPV. It is assumed that most hydrocarbons in the Meramec are primarily present in clay-rich lithologies with limited calcite cement; therefore, total porosity (PHI_{Tot}) was used for volumetric calculations. HCPV was calculated by multiplying pore volume by oil saturation (1-S_w). The resulting P10 (most conservative), P50, and P90 (most optimistic) values of pore volume and HCPV were determined.

Production Analysis

To evaluate the controls that lithology, rock types, and geomechanical properties might have on reservoir performance, 14 producing horizontal wells drilled primarily in parasequences 3 and 4 in the Meramec were evaluated. Lithology, rock-type, Poisson's Ratio, and Young's Modulus logs were extracted along the laterals from the associated 3D models, and the percentages for each of the properties was calculated. The 180-day and 360-day cumulative oil production (STB) was normalized by dividing the cumulative oil production by the lateral length of the well. The percentage of each lithology, rock type, and discrete geomechanical property was compared to the 180-day and 360-day cumulative oil production (STB) normalized to BBL/ft.

RESULTS

Lithologies and Rock Types

Based on core descriptions with petrographic data and calculated mineralogy from X-ray fluorescence, five lithologies were defined within the Mississippian Meramec by Miller (2019): 1) mudstone, 2) argillaceous siltstone, 3) argillaceous-calcareous siltstone, 4) calcareous siltstone, and 5) silty limestone (Table 1) and were used in this study. Other studies from Drummond (2018), Duarte (2018), Hickman (2018), Miller et al. (2019), and Price et al., 2020 describe similar lithologies with varying degrees of bioturbation and sedimentary structures.

Gupta (2018, personal communication) defined 3 rock types: rock type 1, rock type 2, and rock type 3 based on the FZI approach. Rock type 1 has the least carbonate, most clay, lowest Young's Modulus, low brittleness, highest porosity, and exhibits low water saturation. Rock type 3 has the most carbonate, least clay, low porosity, high brittleness, high Young's Modulus, and relatively high water saturation. Rock type 2 is defined as having property values that are between those of rock type 1 and rock type 3.

By means of electrofacies classification using a supervised Artificial Neural Network [ANN] and a log suite consisting Gamma ray (GR), Neutron porosity (NPHI), Bulk density (RhoB), and photoelectric effect (PE), the defined lithologies and rock types were estimated in 44 non-cored wells within the study area generating lithology and rock-type classification logs for each of those wells (Miller, 2019).

Stratigraphic and Structural Framework

The Mississippian Meramec in the study area dips toward the southwest and ranges in thickness from approximately 300 – 400 ft (91 – 122 m). The Meramec is thicker in the southwest part of the study area and thins toward the northeast (Figure 8).

The vertical succession of lithologies and rock types represent several higher-order, upward-shallowing cycles that are commonly capped by marine-flooding surfaces (Figures 3 and

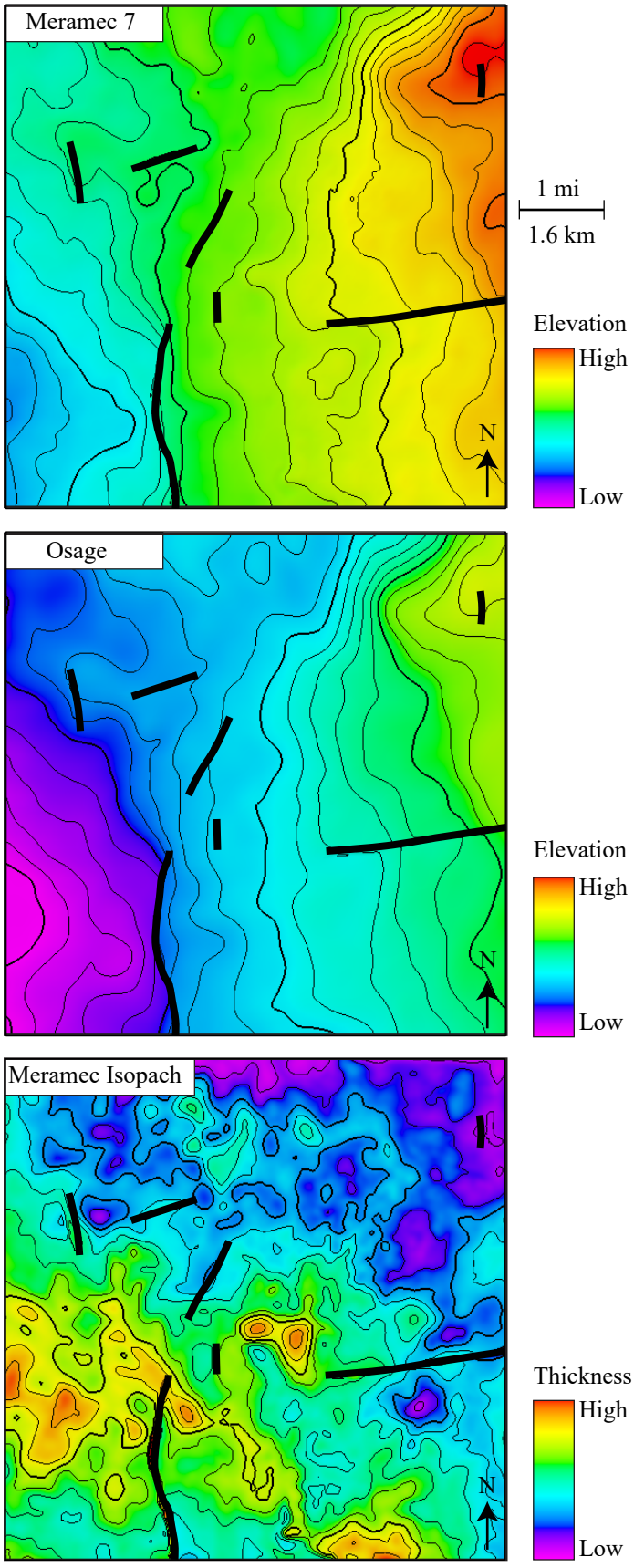
Meramec 7
1 mi
1.6 km
Elevation
High
Low
N
Osage
Elevation
High
Low
N
Meramec Isopach
Thickness
High
Low
N

Figure 8: Structure-contour maps for A) top of Meramec parasequence 7 and B) top of Osage. The Meramec interval is dipping to the southwest. C) Meramec isopach map. The Meramec ranges in thickness from 300 – 400 ft (91 – 122 m) and thickens toward the southwest.

9). These cycles represent parasequences and are generally identified in well logs by an upward decreasing GR signature with a sharp GR increase at the top of each cycle corresponding to the marine-flooding surface (Figures 3 and 9) (Miller, 2019). Controlling factors producing these higher-order cycles are generally attributed to Milankovich-driven eustasy, but additional factors include: tectonics, rate of sedimentation, and short-term climatic variations (Read, 1995; Rogers, 2001; Watney et al., 2001). The Meramec is divided into seven shallowing-upward parasequences based on core-derived lithological stacking patterns, well-log response (GR, NPHI, RhoB, RILD) (Miller, 2019), and seismic data. From base to top, the reservoir zones are referred to as: Meramec 1-7 (Figures 3 and 4).

Seven significant faults extend through the Meramec formation within the study area (Figure 8). In cross-sectional view, the faults appear near-vertical (Figure 4) with offsets ranging from 50 to 150 ft (15 to 46 m). The majority of the faults trend north-south corresponding with the azimuth of the maximum horizontal stress being approximately east-west (N85º(±5º)E) (Alt and Zoback, 2017). Interpreting fault type is difficult due to the small displacement of seismic reflectors and the angle of fault planes; however, most appear as normal or strike-slip. An east-west oriented strike-slip fault is interpreted on the east side of the study area (Figure 8).

P-impedance, S-impedance, and Density

Seismic-to-well ties for 25 vertical wells resulted in cross-correlations ranging between 70% to 85%. The seismic-to-well tie for Well 1 illustrates that the synthetic seismogram correlates well with the surface seismic trace resulting in a cross-correlation of 84% (Figure 6). Well-log and inversion curves follow similar trends with a correlation of 97% within the Meremec interval. A qualitative comparison between the P-impedance values from well logs and

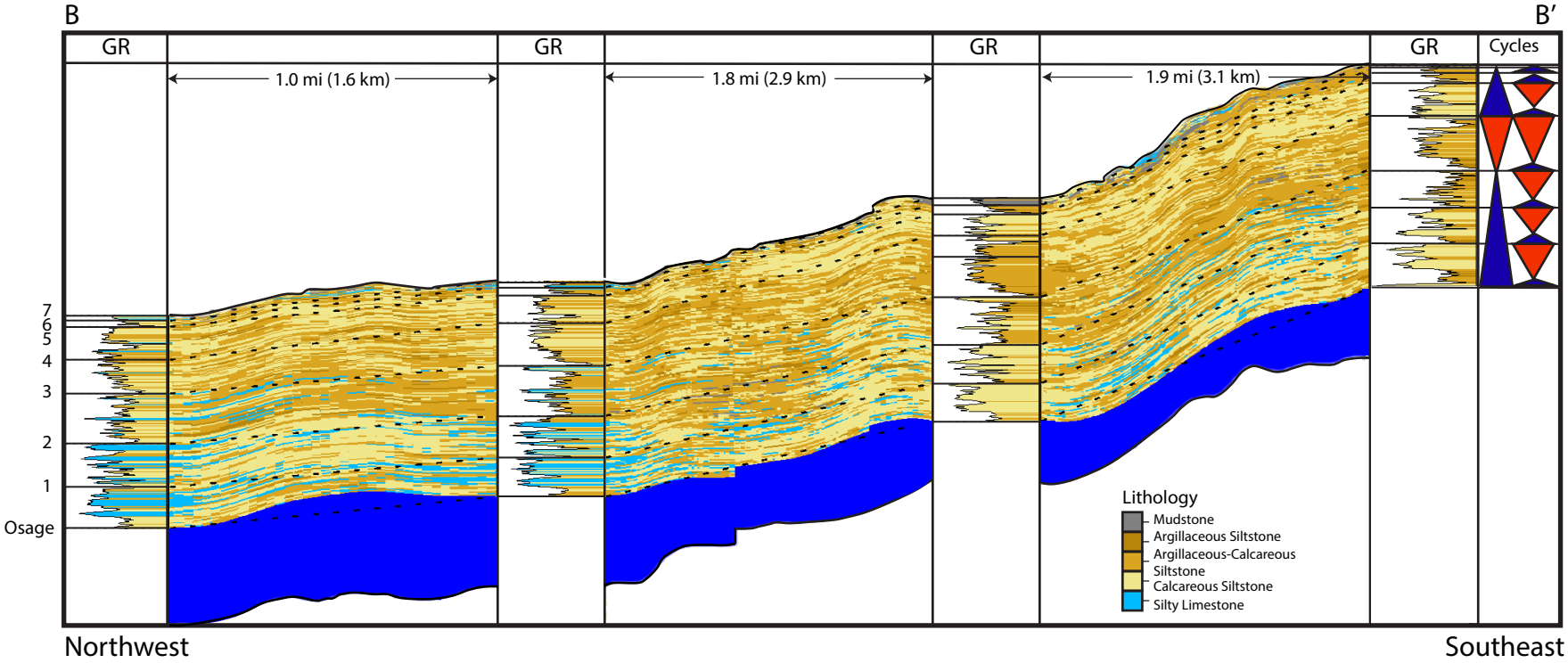

Figure 9: Northwest-southeast oriented well-log and lithology model cross-section (B – B') displaying the Meramec parasequences. The GR track is shaded by lithology and was used to aid in stratigraphic correlation. Moving from the northwest to southwest, the Meramec shallows in structural elevation and the amount of silty limestone diminishes. Location of cross section is shown on Figure 2.

the inversion volume indicates that the inversion accurately estimated the elastic properties at the well locations (Figure 10).

Impedance-based Lithology and Rock-Type Relationships and Probabilities

The predictive capabilities and range of uncertainties of the impedance-based lithology prediction process are illustrated in a confusion matrix (Table 2). It shows that argillaceous-calcareous siltstones are commonly misclassified resulting in an overall accuracy of 55% most likely due to their mixed mineralogy (Appendix-E1). The overall accuracy was greater by combining the argillaceous-calcareous siltstone with the argillaceous siltstone resulting in an overall accuracy of 70%. The confusion matrix for rock types shows an overall accuracy of 79%.

The relationships between the lithologies and rock types and P-impedance and S-impedance are indicated by their associated probability density functions (PDFs). The PDF is represented by a shape that defines the probability of a lithology or rock type being predicting based on their range of impedance values. The resulting PDF shows the probability of predicting each rock type (Figure 11) and lithology (Appendix-E2) according to the combination of its associated P-impedance and S-impedance values. Less overlap and greater separation between each of the rock type or lithology PDFs indicates that the attributes can be used to differentiate between the different classes; thus, increasing the predictive probability. The P-impedance and S-impedance logs create separation between the peaks of the rock type PDFs expressing how each can be represented by different ranges of impedance values.

By applying the lithology and rock-type probabilities defined by the statistical PDFs to the P- and S-impedance seismic attributes, lithology and rock-type classification volumes and probability volumes for each of the lithologies and rock types are generated (Figure 12). The distribution of lithologies and rock-types in the classification volumes demonstrate a direct

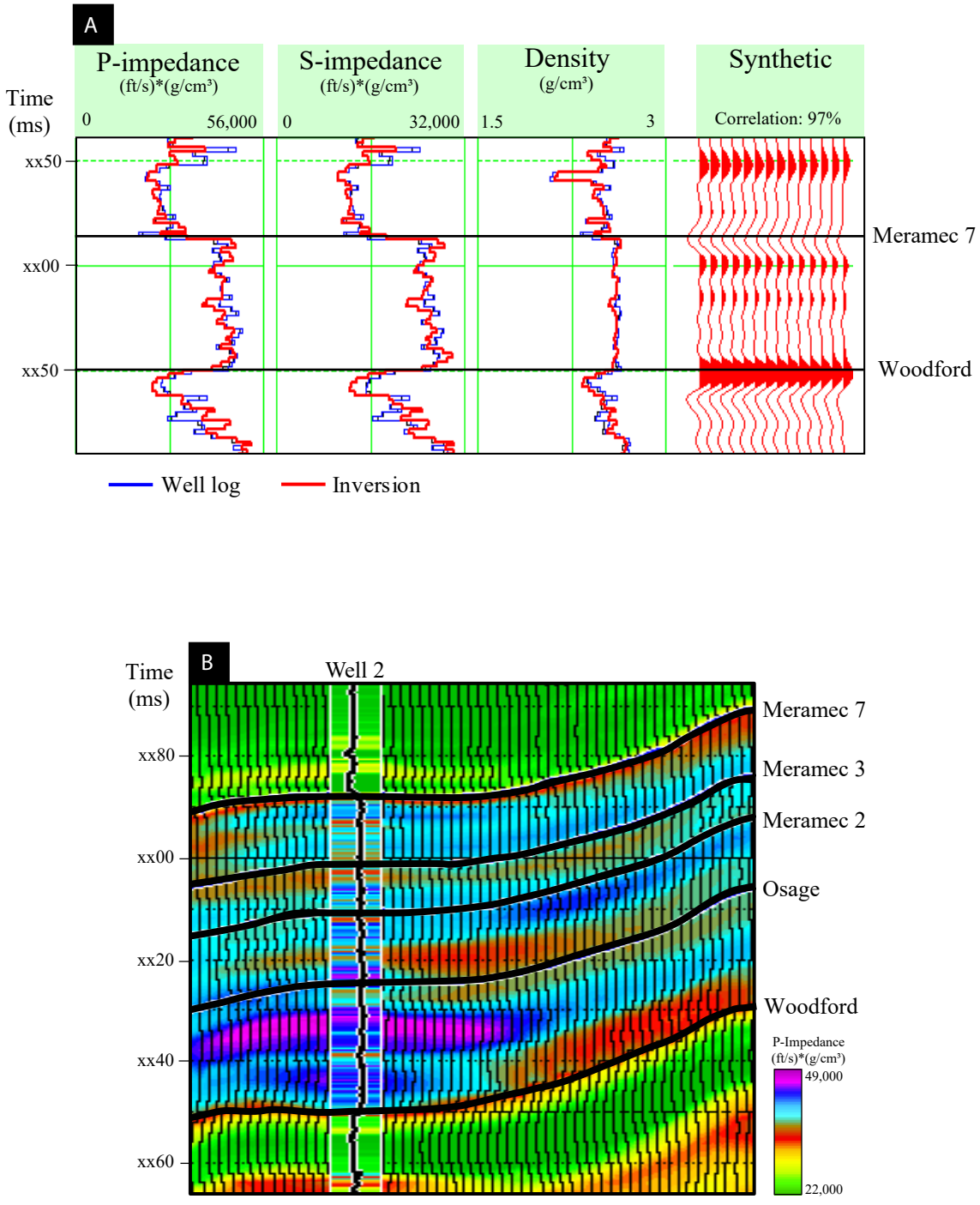

Figure 10: Quantitative and qualitative quality control of the pre-stack inversion results. A) The frequency-filtered P-impedance, S-impedance, and density logs overlying the associated inversion results exhibit a correlation of 97% for Well 2. B) A qualitative comparison showing the p-impedance well log overlying the seismic p-impedance volume with the same color bar.

A

Predicted Lithology	Actual Lithology			
	Mudstone	Argillaceous Siltstone	Calcareous Siltstone	Silty Limestone
Mudstone	89%	15%	0%	0%
Argillaceous Siltstone	11%	67%	20%	1%
Calcareous Siltstone	0%	17%	57%	35%
Silty Limestone	0%	1%	23%	63%
User's Accuracy	**89%**	**67%**	**57%**	**63%**

Overall Accuracy: 70%

B

Predicted Rock Type	Actual Rock Type		
	Rock Type 1	Rock Type 2	Rock Type 3
Rock Type 1	88%	10%	3%
Rock Type 2	9%	72%	19%
Rock Type 3	3%	18%	78%
User's Accuracy	**88%**	**72%**	**78%**

Overall Accuracy: 79%

Table 2: Confusion matrices displaying accuracies for the impedance-based prediction for lithologies and rock types. Argillaceous-calcareous siltstone is combined with argillaceous siltstone to increase the accuracy.

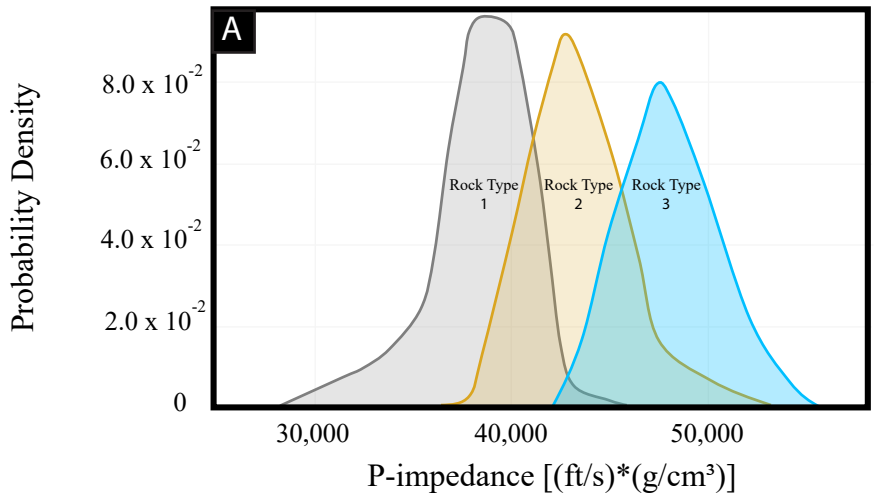
A
Probability Density
8.0 x 10-2
6.0 x 10-2
4.0 x 10-2
2.0 x 10-2
0
Rock Type 1
Rock Type 2
Rock Type 3
30,000
40,000
50,000
P-impedance [(ft/s)*(g/cm³)]

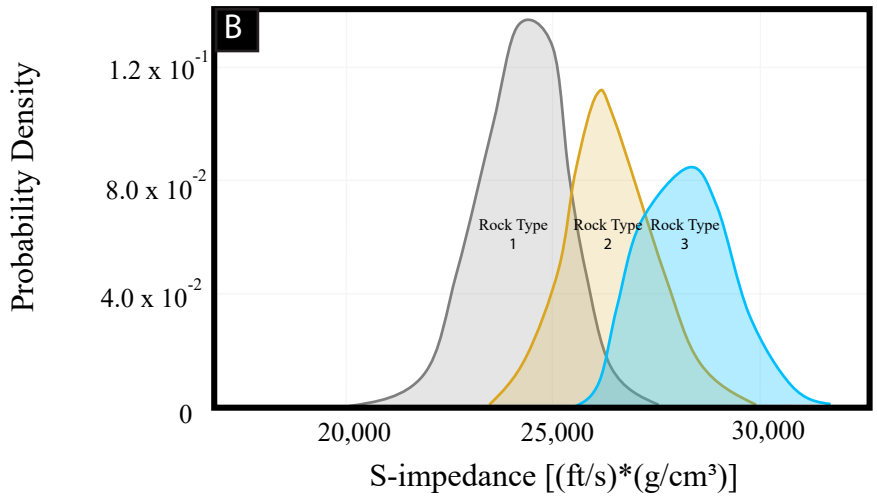
B
Probability Density
1.2 x 10-1
8.0 x 10-2
4.0 x 10-2
0
Rock Type 1
Rock Type 2
Rock Type 3
20,000
25,000
30,000
S-impedance [(ft/s)*(g/cm³)]

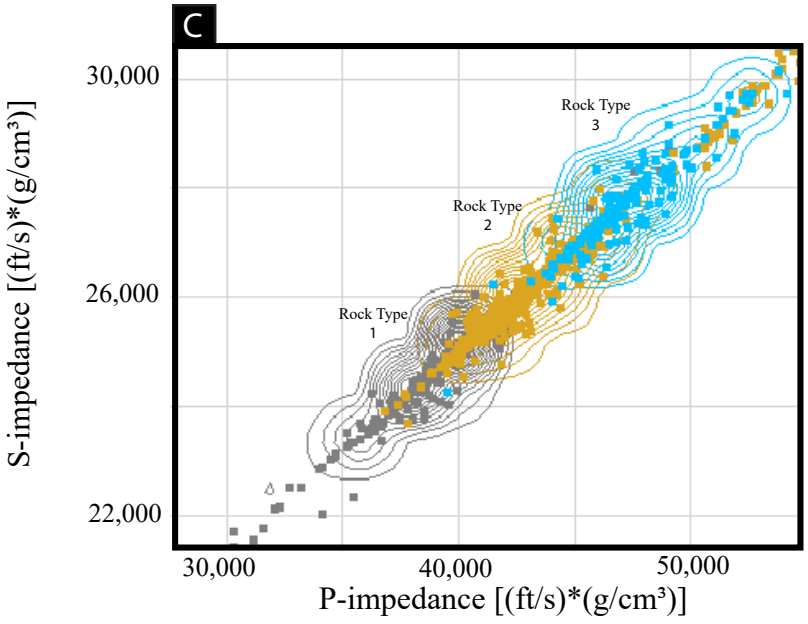
C
S-impedance [(ft/s)*(g/cm³)]
30,000
26,000
22,000
Rock Type 3
Rock Type 2
Rock Type 1
30,000
40,000
50,000
P-impedance [(ft/s)*(g/cm³)]

Figure 11: Probability density functions (PDFs) show the probability of predicting rock types 1, 2, and 3 according to the range of elastic response for each rock type. A) PDFs representing the probability of predicting each rock type according to its p-impedance response. B) PDFs representing the probability of predicting each rock type according to its s-impedance response. C) 3-D PDFs from the combination of the previous plots displaying the probability of predicting each rock type according to its combined p- and s-impedance response.

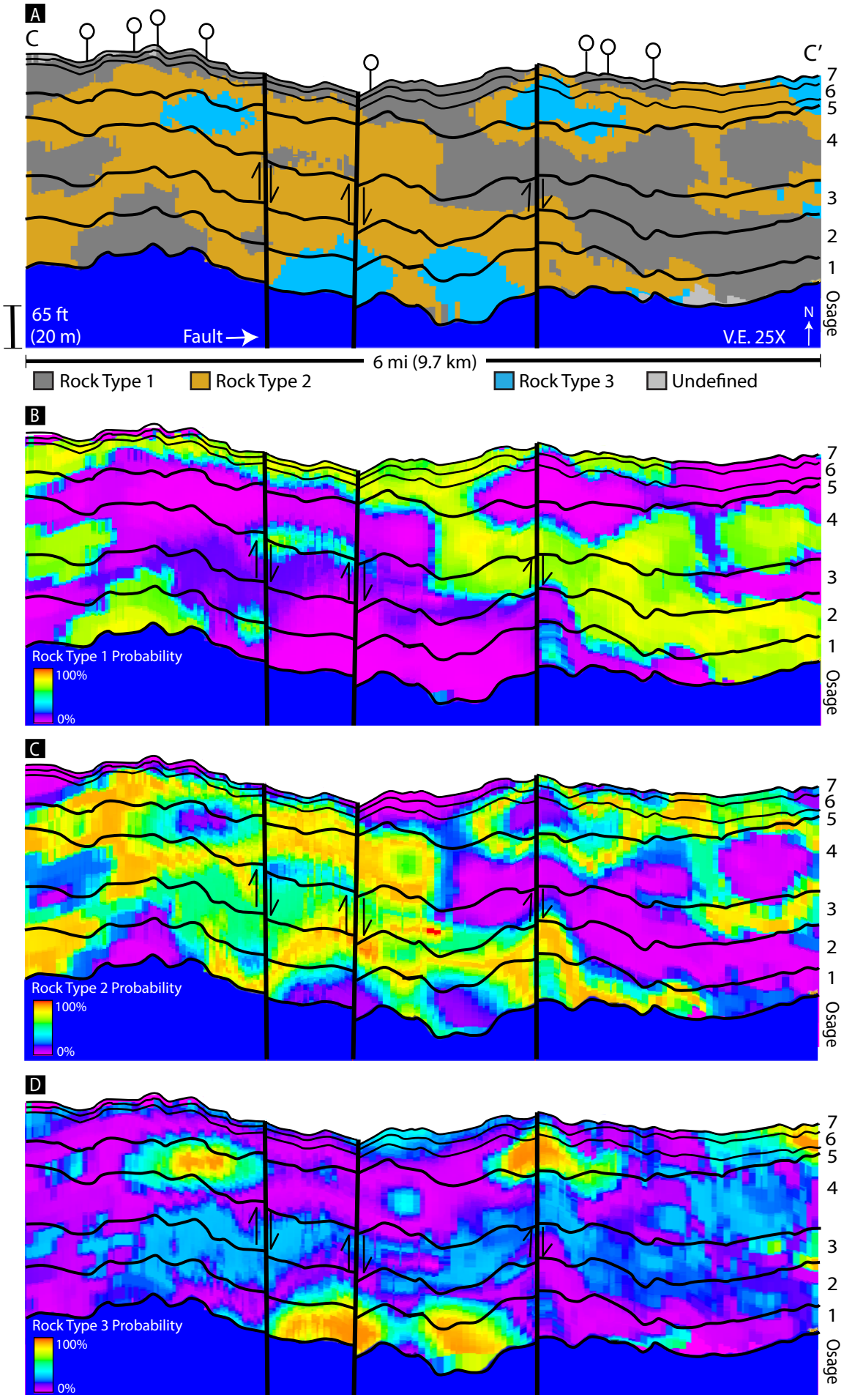
A
C
C′
7
6
5
4
3
2
1
Osage
65 ft
(20 m)
Fault
N
V.E. 25X
6 mi (9.7 km)
Rock Type 1
Rock Type 2
Rock Type 3
Undefined
B
Rock Type 1 Probability
100%
0%
C
Rock Type 2 Probability
100%
0%
D
Rock Type 3 Probability
100%
0%

Figure 12: Northwest-southeast oriented cross-sections (C – C') from the volumes of the impedance-based rock-type prediction and classification process (all flattened on the Woodford Shale): A) most likely rock type present, B) rock type 1 probability, C) rock type 2 probability, and D) rock type 3 probability. The rock type with the highest probability at a specific location is defined as the most likely rock type at that location. Cross-sections illustrate 3 north-south trending faults. Well locations are indicated by white circles. Location of cross section is shown on Figure 2.

correlation to their associated lithology and rock-type probability volumes; where there is the highest probability of a lithology or rock type, it will be defined as that lithology or rock type in the classification volume.

Spatial Distribution of Reservoir Properties

For the Meramec, 30 lithology and 30 rock-type models were generated and evaluated to assess the spatial variability and range of uncertainty of these properties and the associated porosity, water saturation, pore volume, and hydrocarbon pore volume (HCPV) (Figure 13). Variogram parameters for all models are summarized in Appendix-F1 through Appendix-F7.

In terms of lithology, the transition from Meramec parasequences 1, 2, and 3 corresponds to an upward increase from 33% to 66% in argillaceous-rich lithologies and decrease in calcareous-rich lithologies from 67% to 34% (Figures 14) (Appendix-F8). The top of Meramec parasequence 3 represents the maximum flooding surface capping this retrogradational parasequence set (Miller, 2019). Moving stratigraphically upward, an increase in calcareous siltstone (30 to 68%) in Meramec parasequences 4 and 5 suggests these are associated with a progradational parasequence set and coarsening-upward lithology successions. Meramec parasequences 6 and 7 show an increase in argillaceous-rich lithology (30 to 72%) and decrease in calcareous siltstone (68 to 28%) representing a retrogradational parasequence set. Meramec 7 contains the greatest amount of mudstone (26%) within the study area.

In terms of the spatial variability of rock types, parasequences 1, 2, and 3 that form a retrogradrational parasequence set show an upward increase in clay-rich rock type 1 from 5% to 34% and a decrease in the carbonate-rich rock type 3 from 32% to 7% (Figures 13 and 14). Like the lithology model, moving up section from Meramec parasequence 4 to 5, a significant increase in the amount of the calcareous-rich rock type 3 (5 to 43%) is observed. The top of the

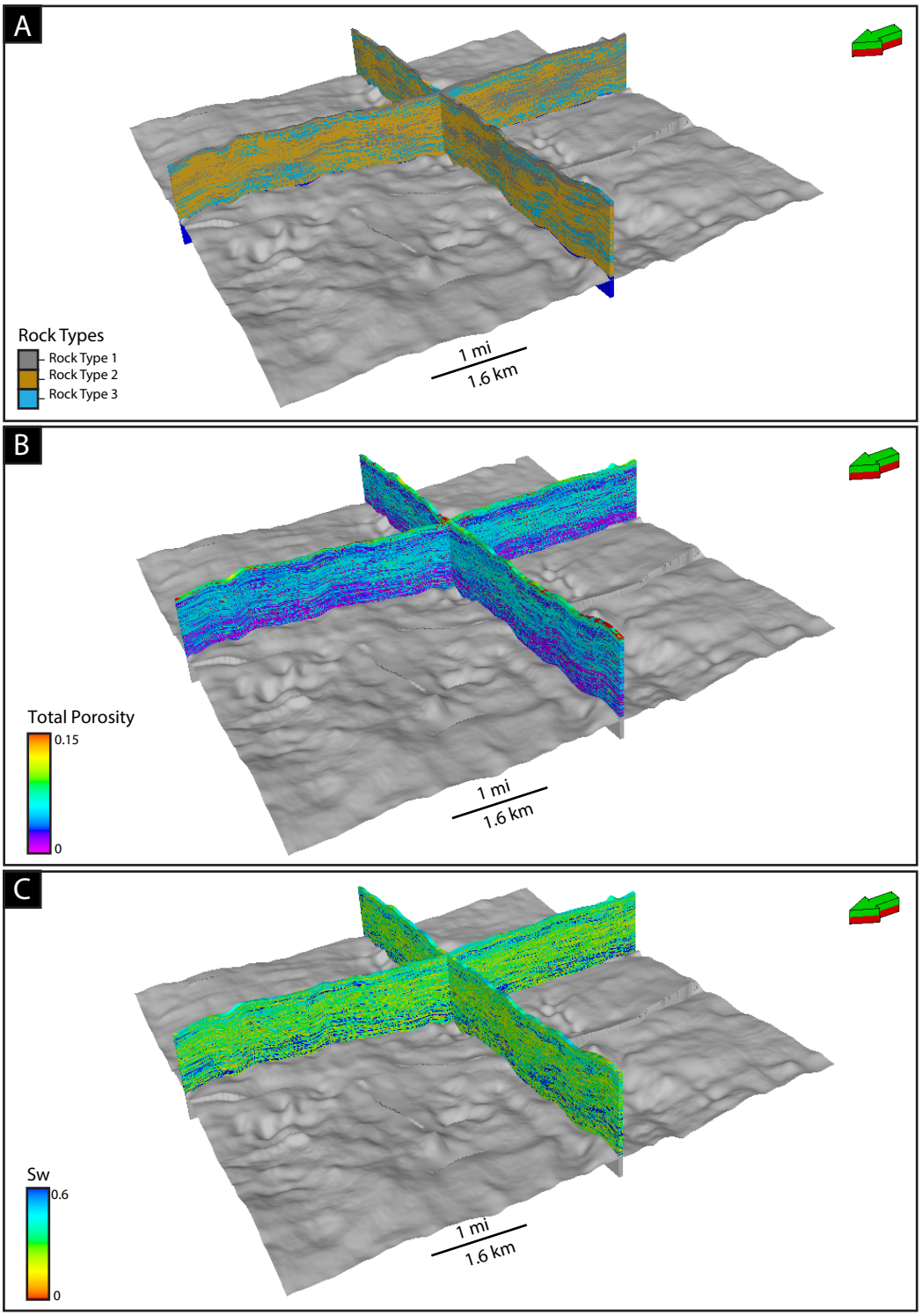

Figure 13: Perspective views of 3D model sections showing the spatial distribution of A) rock types, B) porosity, and C) water saturation. The Osage horizon is displayed. Porosity and water saturation vary with argillaceous-rich and calcareous rich intervals.

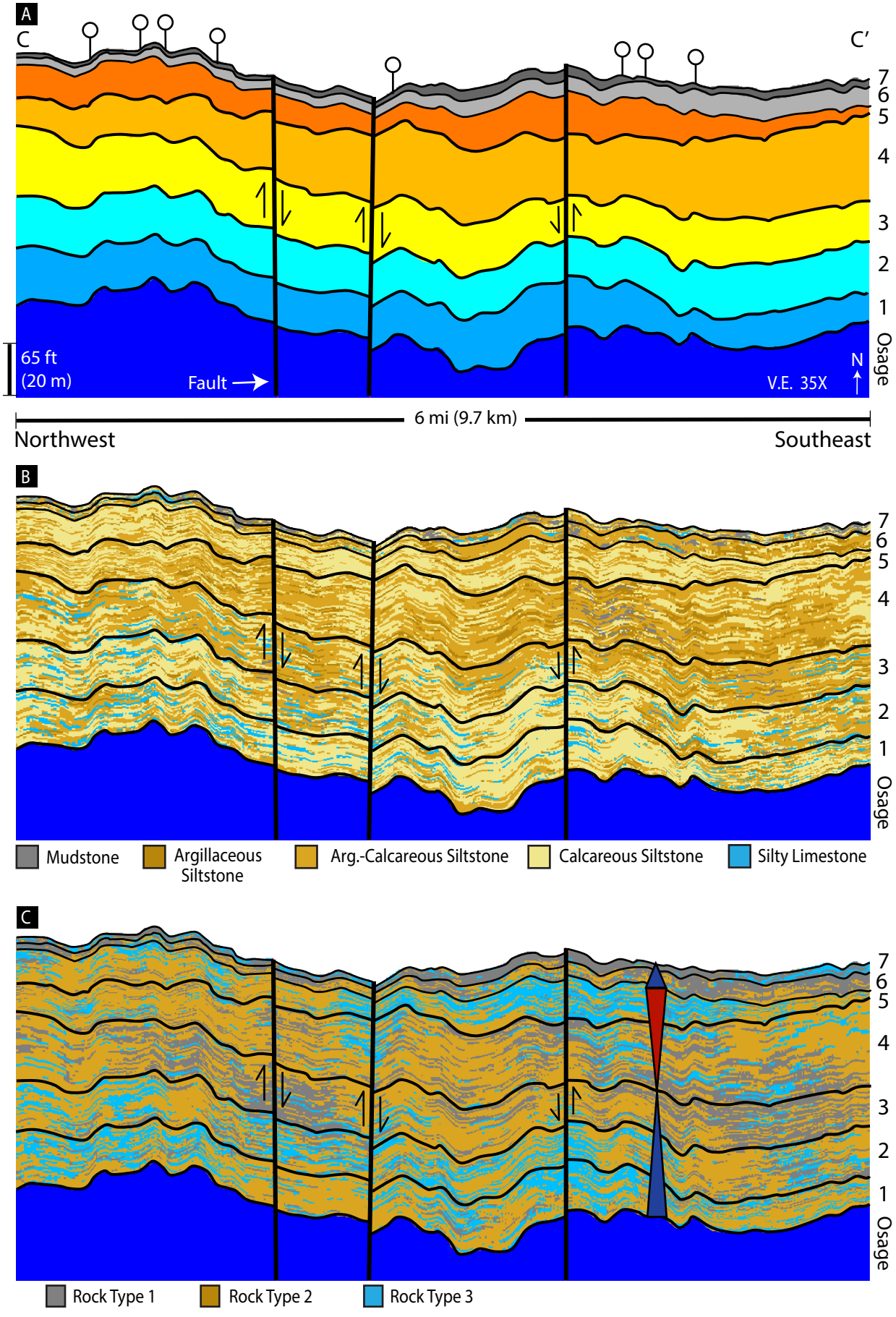
A
C
C'
7
6
5
4
3
2
1
Osage
65 ft
(20 m)
Fault
N
V.E. 35X
6 mi (9.7 km)
Northwest
Southeast
B
Mudstone
Argillaceous Siltstone
Arg.-Calcareous Siltstone
Calcareous Siltstone
Silty Limestone
C
Rock Type 1
Rock Type 2
Rock Type 3

Figure 14: Northwest-southeast oriented cross-sections (C – C') flattened on the Woodford Shale. A) Meramec parasequences. B) Lithology distribution. Moving up section, Meramec 1, 2, and 3 demonstrate an overall increase in argillaceous-rich lithologies and decrease in calcareous-rich lithologies indicative of a retrogradational parasequence set. Meramec parasequences 4 and 5 represent a progradational parasequence set with an upward increase in calcareous-rich lithologies and decrease in clay-rich rocks. Meramec 5 represents a dominantly calcareous interval. Meramec 6 and 7 form a retrogradational parasequence set indicated by a major upward increase in clay-rich lithologies. C) Rock type distribution. The lithology and rock-type models both show retrogradational-progradational-retrogradational trends. Blue and red arrows represent transgressive and regressive stratigraphic cycles, respectively. Well locations are indicated by white circles. Location of cross section is shown on Figure 2.

Meramec containing parasequences 6 and 7 introduce more clay with an increase of rock type 1 (47 to 77%). The lithology and rock-type classifications were created independently of each other yet display a similar retrogradational-progradational-retrogradational trend as also illustrated in the vertical proportion curves for lithologies and rock types (Figure 3).

Total porosity in the Meramec (lithology- and rock-type-based) ranges from 0-15% in the study area (Figures 13 and 15) (Appendix-F8). The rock type-based porosity model shows an upward increase in total porosity moving up section in Meramec parasequences 1, 2, 3, and 4 (mean = 0.2, 3.9, 5.3, and 5.7%, respectively) (Figures 15). Meramec 5 exhibits a lower mean porosity (3.8%) as the calcareous-rich rock type 3 (with more calcite cement) dominates this parasequence. Meramec 6 and 7 have the highest mean total porosity of 6.6% and 7.6%, respectively. The stratigraphic variability of rock-type and lithology-based porosity within the Meramec is similar.

Water saturation (S_w) (lithology- and rock-type-based) is variable with the average being approximately 30-40% in the Meramec (Figures 13 and 15) (Appendix-F8). Parasequences 1, 2, and 3, show higher values of S_w (mean = 39%, 40%, 31%, respectively) (Figure 15). Parasequence 4 has the lowest average S_w (28%). Parasequences 5, 6, and 7 revert to higher average S_w values of 39%, 30%, and 36%, respectively. Like porosity, the lithology-biased S_w shows a similar spatial distribution as rock-type-based water saturation.

Poisson's Ratio (ν) and Young's Modulus (E) are very heterogeneous in the Meramec (Figure 15) (Appendix-F9). Parasequences 4 and 5 exhibit the greatest percentage of the low ν rocks and the high E rocks indicating brittle rock, and this is consistent with the increase in the calcareous-rich lithology and rock type 3. Parasequences 6 and 7 exhibit the greatest percentage

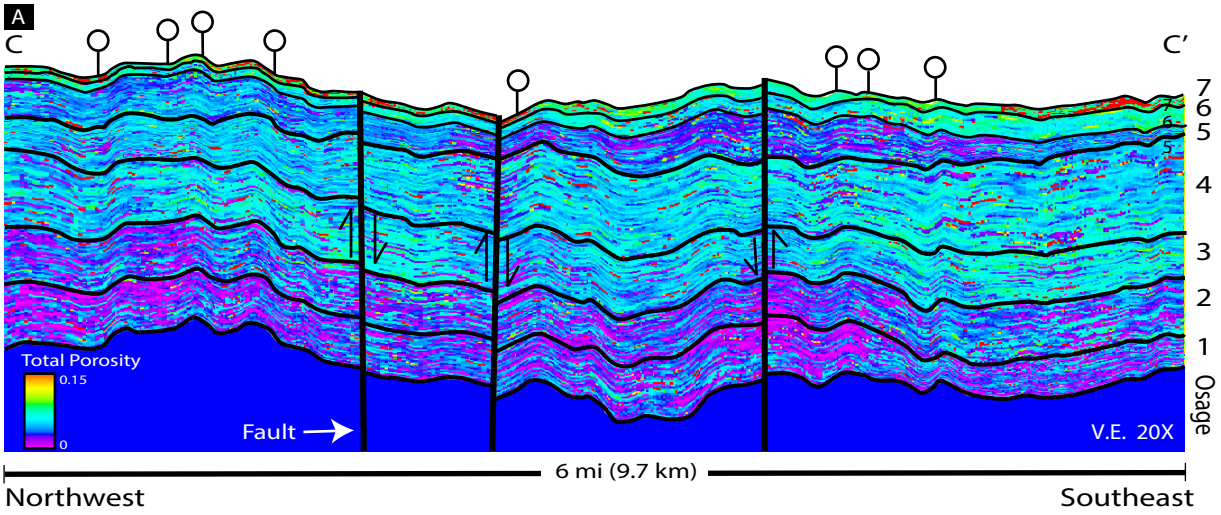
A
C
C'
7
6
5
4
3
2
1
Osage
Total Porosity
0.15
0
Fault
V.E. 20X
6 mi (9.7 km)
Northwest
Southeast

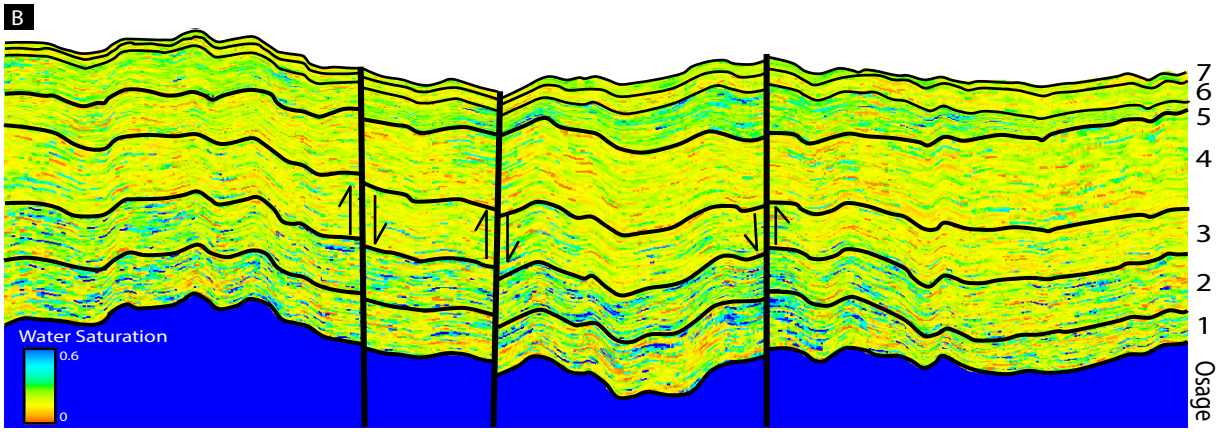
B
7
6
5
4
3
2
1
Osage
Water Saturation
0.6
0

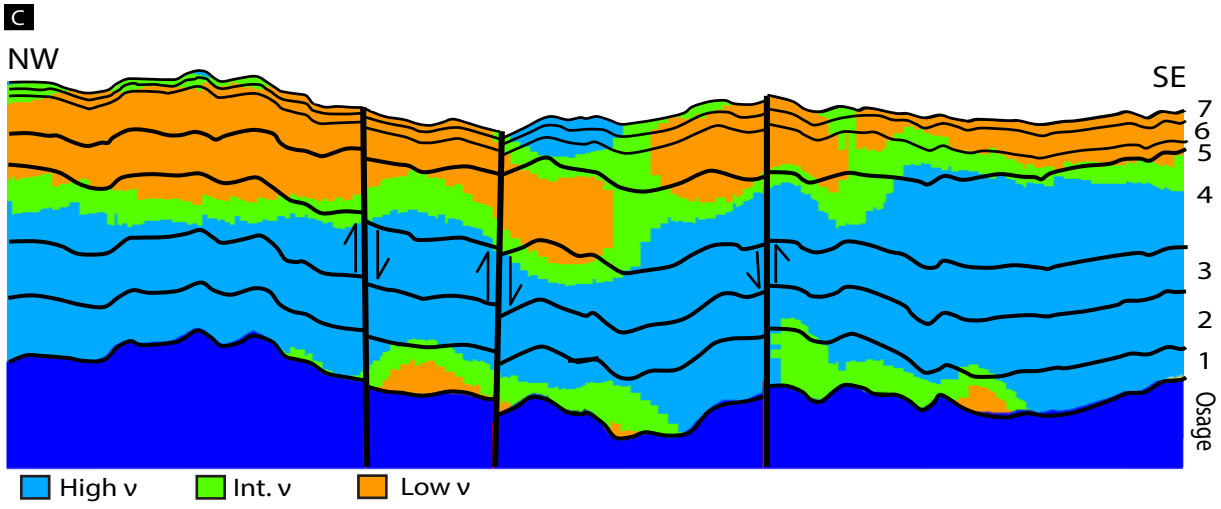
C
NW
SE
7
6
5
4
3
2
1
Osage
High v
Int. v
Low v

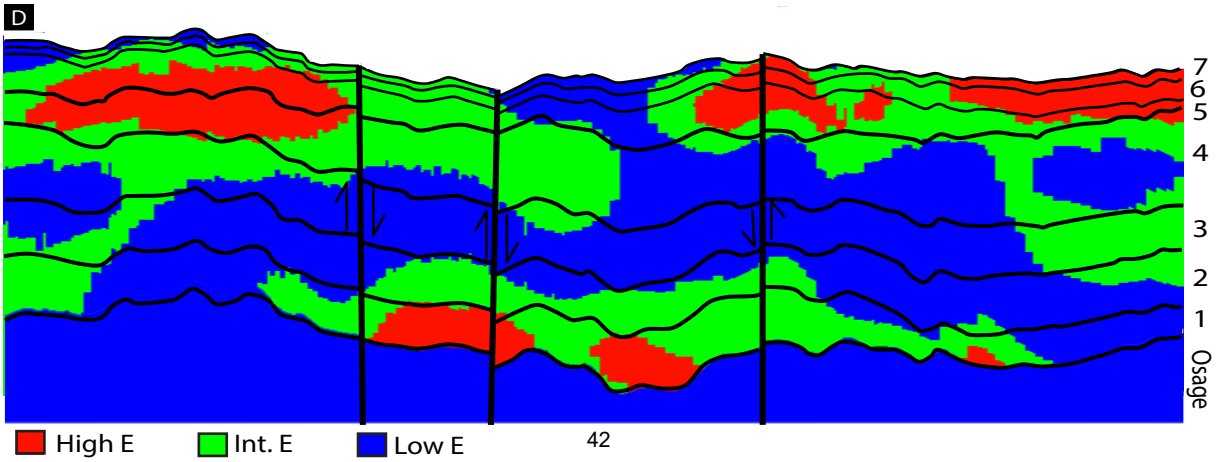
D
7
6
5
4
3
2
1
Osage
High E
Int. E
Low E

Figure 15: Northwest-southeast oriented cross-sections (C – C') flattened on the Woodford Shale. A) Total porosity distribution. An upward increase in porosity occurs from Meramec parasequences 1 to 4 corresponding to the increase in clay-rich lithologies and rock types. A sharp decrease in porosity occurs within the dominantly calcareous parasequence 5. Meramec 6 and 7 show a distinct increase in porosity correlating with the increase of argillaceous-rich lithologies within this retrogradational parasequence set. B) Water saturation distribution. Parasequences 1, 2, 3, and 4 show decreasing values of water saturation as clay-rich lithologies and rock types become more prominent. An increase in water saturation is observed in parasequence 5 and begins to decrease moving up section into parasequences 6 and 7. The distribution of petrophysical properties appears to be influenced by the amount of calcite and clay. High porosity and low water saturation correspond to clay-rich zones, and low porosity and high water saturation are analogous with calcite-rich zones. C) Poisson's Ratio (ν) distribution, and D) Young's Modulus distribution. The geomechanical property models are resampled directly from seismic so they portray a lower resolution as compared to the lithology, rock type, and petrophysical models. Well locations are indicated by white circles. Location of cross section is shown on Figure 2.

of high *v* and low *E* rocks associated with a more ductile interval which corresponds to the presence of more argillaceous-rich lithologies and rock type 1.

Within the study area, the lateral variability of lithologies, rock types, and petrophysical properties appears to be less significant as compared to their stratigraphic variability; thus, the sequence stratigraphy of the Meramec imparts a distinct stratigraphic control on reservoir quality.

Lithology, Rock-Type and Geomechanical Controls on Reservoir Performance

Pore volume and HCPV in reservoir barrels (RB) were generated for the P10 (most conservative volumetric outcome), P50, and P90 (most optimistic volumetric outcome) cases (by zone and total) for both the lithology and rock-type across the study area (Appendix-G1 and Appendix-G2). Parasequences 3 and 4 exhibit the greatest pore volume and HCPV. These intervals also exhibit relatively high porosity and low water saturation values (Figures 15).

The production analysis revealed a negative correlation (R^2 = 54%) between the percentage of argillaceous-rich rock type 1 and 180-day cumulative oil production, and a positive correlation (R^2 = 52%) between the percentage of the intermediate (argillaceous-calcareous) rock type 2 and 180-day cumulative oil production (Figure 16). A trend is not observed between the calcareous-rich rock type 3 and cumulative oil production data. The same correlations are observed for rock-type percentage and normalized 360-day cumulative production. However, no trends are observed regarding the percentage of lithology and 180-day and 360-day cumulative production (Appendix-H1). These comparisons show that the high-clay content rock type 1 is associated with relatively poor reservoir quality, and the argillaceous-calcareous mixed rock type 2 is associated with a higher quality reservoir rock.

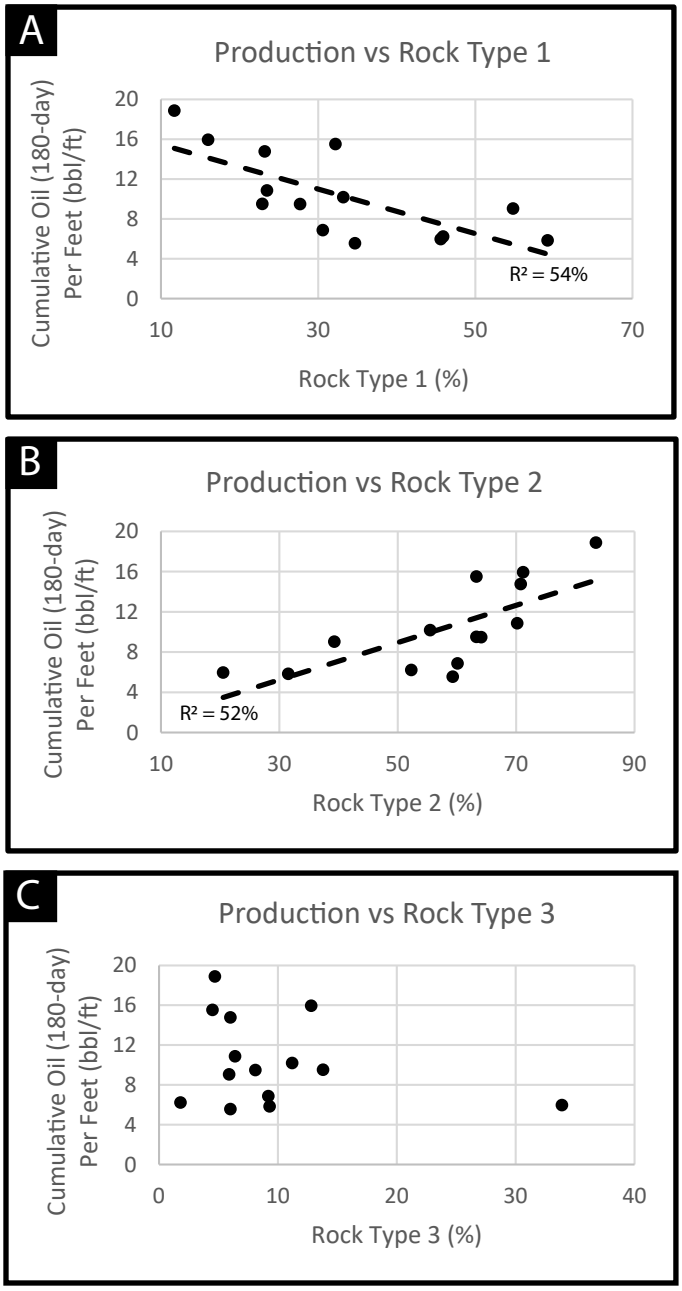

Figure 16: Cross plots of cumulative oil production vs. rock type. 180-day cumulative oil production are compared to the percentage of rock types along the lateral of 13 producing horizontal wells. A negative correlation between rock type 1 and production is observed, while rock type 2 shows a positive correlation with production. No correlation is determined when comparing rock type 3 and production.

The comparison of geomechanical properties with normalized 180-day oil production (Figure 17) reveal a positive correlation (R^2 = 70%) between the abundance of high *E* (brittle) rock and production, and a negative correlation (R^2 = 54%) between the percentage of low *E* (ductile) rock and well production. Similarly, a positive correlation (R^2 = 66%) is observed between the abundance of low *v* (brittle) rock and the amount of oil production, and a negative correlation (R^2 = 56%) between the percentage of high *v* (ductile) rock and well production. Production drivers from this analysis correspond to reservoir rocks that are more brittle in nature as indicated by the combination of relatively high Young's Modulus and low Poisson's Ratio.

DISCUSSION

Seismic Integrated Reservoir Modeling of the Meramec

Integrated reservoir models require the incorporation of all available data from multiple disciplines including geology, geophysics, petrophysics, and rock physics. The integration of seismic data adds value to the accuracy of the reservoir models by helping to define the structural and stratigraphic framework of the area through the incorporation of interpreted faults and reservoir parasequence horizons. The seismic data also add a lateral constraint to the distribution of lithological and petrophysical properties by using the pre-stack inversion results to guide the distribution of rock properties within the model framework. The geomechanical properties derived from the pre-stack inversion provided more information about the distribution of brittle and ductile properties within the Meramec. Overall, the incorporation of the seismic data into the reservoir modeling adds spatial constraints improving the analysis of the Meramec structure, stratigraphy, and distribution of rock properties within the study area.

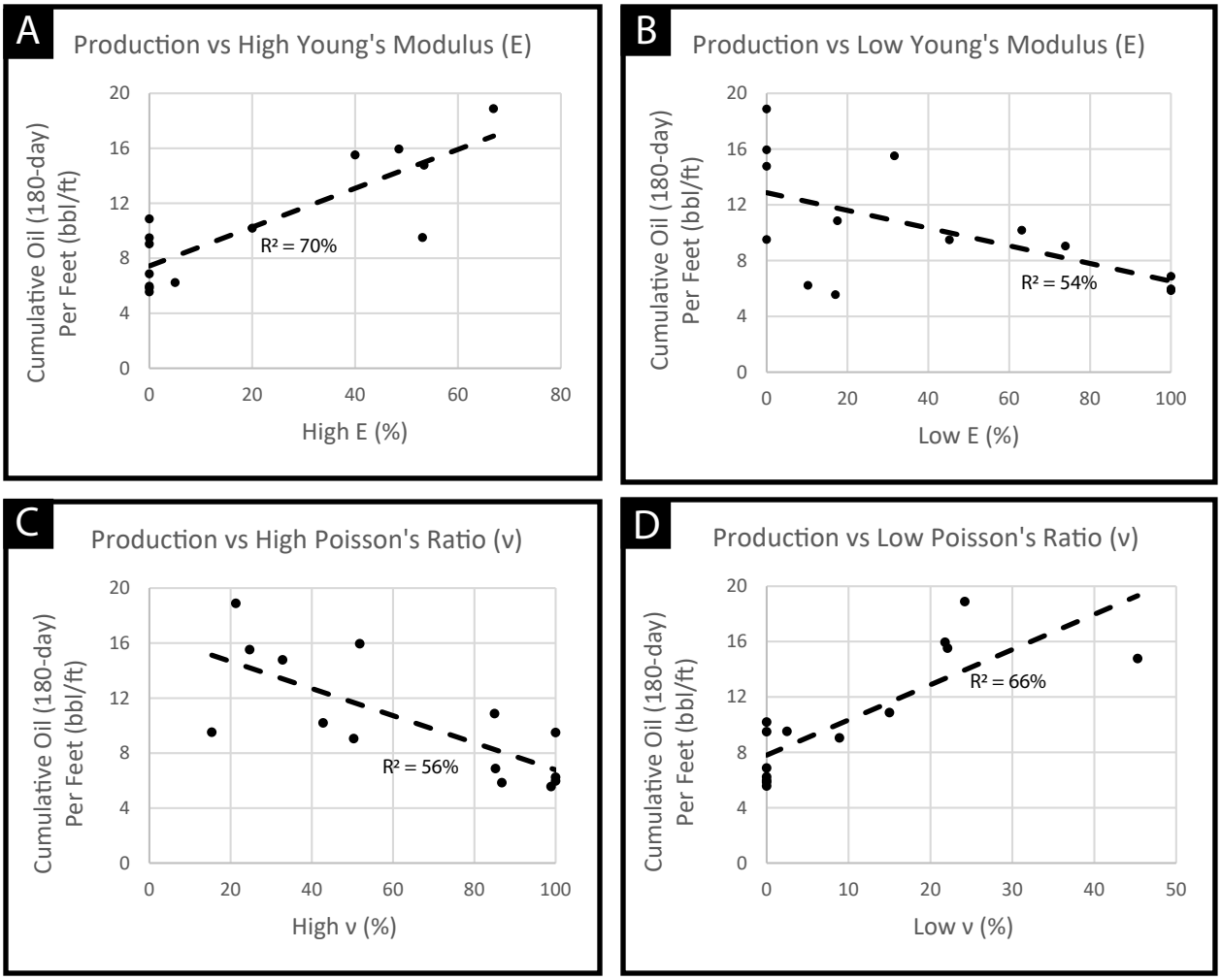

Figure 17: Cross plots of cumulative oil production vs. geomechanical properties. 180-day cumulative oil production are compared to Poisson's Ratio (*v*) and Young's Modulus (*E*) along the lateral of 13 producing horizontal wells. The results show a positive correlation between both high *E* and low *v* and production, and a negative correlation between both low *E* and high *v* and production. This indicates that relatively more brittle rocks are related to high reservoir quality.

Production Drivers

The reservoir quality, typically defined by hydrocarbon storage capacity and deliverability, is variable within the Meramec. Previous studies suggest that the dominant drivers of reservoir quality within this low porosity and low permeable rock are related to the volume of clay and calcite cement within the reservoir (e.g., Hardwick, 2018; Miller, 2019; Price et al., 2020). Hence, the more argillaceous-rich siltstone is defined as the better reservoir rock due to the ability of clay to line the inner pores, limiting calcite cement, and preserving primary porosity. Also, zones of higher porosity and permeability within the Meramec can be associated with abundant open fractures in the more brittle rock, and low porosity zones are characterized by cemented and healed fractures (Xiaoxuan, 2019). Comparisons of reservoir properties to oil production data from 14 wells primarily targeting parasequences 3 and 4 show that rock type 2 and more brittle rocks appear to be related to high reservoir quality and a driver of oil production (Figures 17 and 18). While rock type 1 (more ductile rocks) are associated with relatively lower reservoir quality. These results suggest an over-abundance of clay and highly ductile rock in the Meramec reservoir is disadvantageous as confirmed with the negative production correlation with clay-rich rock type 1 and ductility. Drilling with freshwater mud also causes clays to swell; thus, occluding porosity. Hydraulic fracturing will not be as effective in highly ductile rocks as increased brittleness allows for more rock volume to be stimulated during horizontal well completions. The mixed mineralogical components of rock type 2 correspond to appropriate amounts of clay with limited calcite cement; thus preserving primary porosity (Price et al., 2017; Hardwick, 2018; Miller, 2019; Price et al., 2020), and the calcareous mineralogy adds a brittle component to the reservoir rock. The brittle nature enhances the possible presence of natural fractures and is more favorable to drill and hydraulically fracture. Therefore, rock type 2 exhibits

an ideal balance in regard to mineralogy making it a more ideal reservoir rock in terms of pore volume and brittleness.

Stratigraphic Controls on Reservoir Quality

Mississippian Meramec strata exhibit a multi-fold sequence-stratigraphic control on reservoir quality (Drummond, 2018; Miller, 2018, Hardisty, 2019; Miller, 2019; Price et al., 2020). Meramec parasequences with an abundance of rock type 2 and more brittle rocks (high E, low *v*) are associated with relatively higher reservoir quality. The most abundant distribution of rock type 2 throughout the Meramec is within parasequences 3 and 4, which corresponds to higher average total porosity (mean = 5.3 % and 5.7 %, respectively) and lower average water saturation (mean = 31 % and 28 %, respectively). The Meramec parasequences 3 and 4 align above and below the maximum flooding surface indicating a period of transition from a transgressive to regressive environment within the rise-fall-rise cycle. Parasequences 4 and 5 reveal the greatest percentage of the more brittle (high *E*, low *v*) rock and are associated with a coarsening-upward progradational parasequence set. Although, parasequence 5 is likely an interval of lower reservoir quality as it is dominated by calcareous-rich lithologies associated with lower average porosity (mean = 3.8 %) presumably caused by a relative drop in sea level resulting in the seaward migration of wave base and increase in calcareous input (Price et al., 2020). Along with the higher order cycles, vertical succession lithologies and rock types in the Meramec show an overall increase in clay and decrease in calcite corresponding to an overall relative rise in sea level (Figure 3). The overall deepening resulted in Meramec parasequences 6 and 7 to contain an abundance of rock type 1 and are ductile (low E, high *v*). High average values of water saturation (mean = 35 % and 36 %, respectively) are also observed within these parasequences. Due to the association of Meramec parasequences 6 and 7 with rock type 1, more

ductile rocks, and high water saturation, the reservoir quality is relatively low in comparison to parasequences 3 and 4. The stacking pattern and distribution of lithologies and rock types indicate a stratigraphic control on the distribution of optimal reservoir quality parameters including geomechanical and petrophysical properties.

CONCLUSIONS

The Mississippian Meramec strata within the STACK play of central Oklahoma is a fine-grained system composed of carbonate and siliciclastic deposits that were deposited on a regionally extensive ramp and basin-floor setting of the Anadarko Basin. The complex stacking pattern and lateral distribution of lithologies within the Meramec is attributed to relative changes in sea level that impacted the ramp. The Meramec is comprised of five lithologies, including mudstone, argillaceous siltstone, argillaceous-calcareous siltstone, calcareous siltstone, and silty limestone, and three petrophysical rock types. A supervised Artificial Neural Network (ANN) based on well-log and core data was used classify the lithologies and rock types in non-cored wells throughout the study area. The Meramec interval within the study area dips to the southwest and ranges in thickness from 300 – 400 ft (91 – 122 m) with thicker Meramec sediment packages in the southwest and thinner toward the northeast. In the study area, the Meramec exhibits as many as seven parasequences and is cut by 7 faults with displacement ranging from 50 – 150 ft (15 – 46 m).

A pre-stack inversion yielded P-impedance, S-impedance, and density volumes, and were combined to construct geomechanical estimates of Poisson's Ratio and Young's Modulus. The spatial distribution of rock properties within the Meramec are demonstrated in the seismic-constrained lithology and rock-type, petrophysical, and geomechanical property models. The

stacking pattern of the parasequences control the distribution of lithologies and rock types impacting the distribution of optimal reservoir quality parameters such as total porosity, water satuation, and geomechanical properties.

Production analysis reveal the drivers of high productivity are associated with rock type 2 and the more brittle rock. Rock type 2 exhibits an ideal balance in regard to mineralogy making it a more ideal reservoir rock in terms of pore volume and brittleness. The distribution of optimal reservoir quality parameters including geomechanical and petrophysical properties are associated with the stratigraphically controlled stacking pattern and distribution of lithologies and rock types. Meramec parasequences 3 and 4 consist of higher distributions of rock type 2, average total porosity, average pore volume and HCPV, and lower water saturation with parasequence 4 also containing a high percentage of the more brittle rock. This suggests that parasequences 3 and 4 have the depositional, petrophysical, and geomechanical characteristics associated with higher reservoir quality within the Meramec.

REFERENCES

Aki, K., and Richards, P.G., 2002, Quantitative Seismology, 2nd Edition: W.H. Freeman and Company.

Alt, R. C., and M. D. Zoback, 2017, In Situ Stress and Active Faulting in Oklahoma: Bulletin of the Seismological Society of America, **107**, 1–36.

Amaefule, J., M. Altunbay, D. Tiab, D. Kersey, and D. Keelan, 1993, Enhanced reservoir description: Using core and log data to identify hydraulic (flow) units and predict permeability in un-cored intervals/wells: Proceedings of SPE Annual Technical Conference and Exhibition, doi:10.2523/26436-ms.

Bachrach, R., M. Beller, C. C. Liu, J. Perdomo, D. Shelander, and N. Dutta, 2004, Combining rock physics analysis, full waveform prestack inversion, and high resolution seismic interpretation to map lithology units in deep water: A Gulf of Mexico case study: The Leading Edge, 378–383.

Ball, M. M., M. E. Henry, and S. E. Frezon, 1991, Petroleum Geology of the Anadarko Basin Region, Province (115), Kansas, Oklahoma, and Texas: USGS Open-File Report 88-450W, 1–36.

Barclay, F., J. C. Alfaro, A. Bruun, A. Cooke, D. Cooke, R. Godfrey, J. Herwanger, D. Lowden, S. McHugo, A. Murineddu, H. Ozdemir, S. Pickering, F. G. Pineda, D. Salter, K. B. Rasmussen, A. Rasmussen, R. Roberts, and S. Volterrani, 2008, Seismic Inversion: Reading between the lines: Oilfield Review, 42–63.

Barnes, A. E., 2007, A tutorial on complex seismic trace analysis: Geophysics, **72**, W33–W43.

Beebe, B. W., 1959, Characteristics of Mississippian Production in the Northwestern Anadarko Basin: Tulsa Geological Society Digest, **27**, 190–205.

Blakey, R., 2011, Paleogeography and geologic evolution of North America, http://jan.ucc.nau.edu/~rcb7/index.html.

Boyd, D. T., 2008, Stratigraphic guide to Oklahoma oil and gas reservoirs: Oklahoma Geological Society, Special Publication 2008-1, 1–2.

Cahill, T. E., 2014, Subsurface Sequence Stratigraphy and Reservoir Characterization of the Mississippian Limestone (Kinderhookian to Meramecian), South Central Kansas and North Central Oklahoma, M.S. thesis, University of Arkansas.

Campbell, J. A., C. J. Mankin, A. B. Schwarzkopf, and J. J. Raymer, 1988, Habitat of petroleum in Permian rocks of the Midcontinent region; in, Permian Rocks of the Midcontinent, W. A. Morgan and J. A. Babcock, eds.: Midcontinent Society of Economic Paleontologists and Mineralogists, Special Publication No. 1, 13–35.

Comer, J. B., 1991, Stratigraphic Analysis of the Upper Devonian Woodford Formation, Permian Basin, West Texas and Southeastern New Mexico: Bureau of Economic Geology Report of Investigations, **201**, 20–35.

Curtis, D. M., and S. C. Champlin, 1959, Depositional Environments of Mississippian Limestones of Oklahoma: Tulsa Geological Society Digest, **27**, 90–103.

Doll, P. L., 2015, Determining structural influence on depositional sequences in carbonates using core-calibrated wireline logs: Mississippian, Mid-continent, U.S.A., M.S. thesis, Oklahoma State University.

Dowdell, B. L., J. T. Kwiatkowski, and K. J. Marfurt, 2013, Seismic characterization of a Mississippi Lime resource play in Osage County, Oklahoma, USA: Interpretation, SB97–SB108.

Drummond, K., 2018, Regional stratigraphy and proximal to distal variation of lithology and porosity within a mixed carbonate-siliciclastic system, Meramec and Osage series (Mississippian), central Oklahoma, M.S. thesis, University of Oklahoma.

Duarte, D. E., 2018, Rock characterization and stratigraphy of the Mississippian strata Meramec/Sycamore Merge play, central Oklahoma, M.S. thesis, University of Oklahoma.

Dutton, S. P., 1984, Fan-Delta Granite Wash of the Texas Panhandle: Oklahoma City Geological Society, Short Course Notes, 1–44.

Etris, E. L., N. J. Crabtree, and J. Dewar, 2002, True Depth Conversion: More Than a Pretty Picture: CSEG Recorder, **26**, no. 9, 1–19.

Fatti, J. L., P. J. Vail, G. C. Smith, P. J. Strauss, and P. R. Levitt, 1994, Detection of gas in sandstone reservoirs using AVO analysis: A 3-D seismic case history using the geostack technique: Geophysics, **59**, 1362–1376, doi: 10.1190/1.1443695.

Gallardo, J., and D. D. Blackwell, 1999, Thermal Structure of the Anadarko Basin: AAPG Bulletin, **83**, 333–361.

Goodway, W., T. Chen, and J. Downton, 1997, Improved AVO fluid detection and lithology discrimination using Lamé petrophysical parameters: 67th Annual International Meeting, SEG, Expanded Abstracts, 183–186.

Grammer, G. M., D. Boardman, J. Puckette, J. Gregg, J. Priyank., M. Childress, B. J. Price, B. Vanden Berg, and S. LeBlanc, 2013, Integrated reservoir characterization of Mississippian Age Midcontinent carbonates: AAPG Search and Discovery Article #30297, 1–31.

Ham, W. E., and J. L. Wilson, 1967, Paleozoic Epeirogeny and Orogeny in the Central United States: American Journal of Science, **265**, 332–407.

Hampson, D. P., B. H. Russell, and B., Bankhead, 2006, Simultaneous Inversion of Pre-stack Seismic Data: Geohorizons, 13–17.

Han, H., J. C. Acosta, S. Dang, J. Fu, C. S. Rai, and C. Sondergeld, 2019, X-ray Fluorescence and Laser Induced Breakdown Spectroscopy for Advanced Rock Elemental Analysis: Unconventional Resources Technology Conference (URTEC), Article #1072, 1–12.

Haq, B. U., and S. R. Shutter, 2008, A Chronology of Paleozoic Sea-Level Changes: AAAS Science, **322**, 64–68.

Hardisty, L., 2019, Stratigraphic variability of Mississippian Meramec chemofacies and petrophysical properties using machine learning and geostatistical modeling, STACK trend, Anadarko Basin, Oklahoma, M.S. thesis, University of Oklahoma.

Hardwick, J., 2018, Reservoir quality evaluation of the Meramec and Upper Osage units in the Anadarko Basin, M.S. thesis, University of Oklahoma.

Hickman, G., 2018, Parasequence-scale stratigraphic variability of lithology and porosity of Mississippian Meramec reservoirs and the relationships to production characteristics, STACK trend, Oklahoma, M.S. thesis, University of Oklahoma.

Johnson, K. S., and K. V. Luza, 2008, Earth sciences and mineral resources of Oklahoma: Oklahoma Geological Survey, Educational Publication 9, 1–22.

Kay, S. M., 1993, Fundamentals of Statistical Signal Processing: Estimation Theory: Prentice Hall PTR.

LeBlanc, S. E., 2014, High resolution sequence stratigraphy and reservoir characterization of the “Mississippian Limestone” in north-central Oklahoma, M.S. thesis, Oklahoma State University.

Lindzey, K. M., M. J. Pranter, and K. J. Marfurt, 2019, Lithological and petrophysical controls on production of the Mississippian limestone, northeastern Woods County, Oklahoma, in G. M. Grammer, J. M. Gregg, J. O. Puckette, P. Jaiswal, S. J. Mazzullo, M. J. Pranter, and R. H. Goldstein, eds., Mississippian reservoirs of the midcontinent: AAPG Memoir 122, 541–560.

LoCricchio, E., 2012, Wash Play Overview, Anadarko Basin: Stratigraphic framework and controls on Pennsylvanian granite wash production, Anadarko Basin, Texas and Oklahoma: AAPG Search and Discovery Article #110163.

Mazzullo, S. J., 2011, Mississippian oil reservoirs in the southern Midcontinent: new exploration concepts for a mature reservoir objective: AAPG Search and Discovery Article #10373.

Mazzullo, S. J., B. W. Wilhite, D. R. Boardman, B. T. Morris., and C. J. Godwin, 2016, Stratigraphic architecture and petroleum reservoirs in lower to middle Mississippian strata (Kinderhookian to basal Meramecian) in subsurface central to southern Kansas and northern Oklahoma: Shale Shaker, **67**, no. 2, 20–49.

McConnell, D. A., M. J. Goyda, G. N. Smith, and J. P. Chitwood, 1989, Morphology of the frontal fault zone, southwest Oklahoma: Implications for deformation and deposition on the Wichita Uplift and Anadarko Basin: Geology, **18**, no. 7, 34–637.

Miller, J. C., M. J. Pranter, and A. B. Cullen, 2019, Regional Stratigraphy and Organic Richness of the Mississippian Meramec and Associated Strata, Anadarko basin, Central Oklahoma: Shale Shaker, **70**, no, 2, 50–79

Miller, M., 2019, Mississippian Meramec Lithologies and Petrophysical Property Variability, STACK Trend, Anadarko Basin, M.S. thesis, University of Oklahoma.

Montgomery, S. L., J. C. Mullarkey, M. W. Longman, W. M. Colleary, and J. P. Rogers, 1998, Mississippian Chat reservoirs, South Kansas: Low resistivity Pay in a Complex Chert reservoir: AAPG Bulletin, **82**, no. 2, 187–205.

Northcutt, R. A., and J. A. Campbell, 1995, Geology provinces of Oklahoma: Oklahoma Geological Survey Open-File Report 5–95.

Northcutt, R. A., K. S. Johnson, and G. C. Hinshaw, 2001, Geology and petroleum reservoirs in Silurian, Devonian, and Mississippian rocks in Oklahoma: Oklahoma Geological Survey Circular 105, 1–15.

Parham, K. D., and R. A. Northcutt, 1993, Mississippian chert and carbonate and basal Pennsylvanian sandstone – central Kansas uplift and northern Oklahoma in D. Bebout, W. White, andpee T. Hentz, eds., Atlas of major Midcontinent gas reservoirs: Gas Research Institute, Bureau of Economic Geology, 57–59.

Peeler, J. A., 1985, Reservoir characterization of the Mississippian “chat,” Hardtner field, southern Barber County, Kansas: M.S. thesis, Wichita State University.

Perry, W. J., 1990, Tectonic Evolution of the Anadarko Basin Region, Oklahoma: U.S. Geological Survey Bulletin, no. 1866-A, A1–A19.

Price, B., K. Haustveit, and A. Lamb, 2017, Influence of Stratigraphy on Barriers to Fracture Growth and Completion Optimization in the Meramec Stack Play, Anadarko Basin, Oklahoma: Unconventional Resources Technology Conference (URTEC), Article #2697585, 1–8.

Price, B. J., and G. M. Grammer, 2018, High resolution sequence stratigraphic architecture and reservoir characterization of the Mississippian Burlington/Keokuk Formation, northwestern Arkansas, in G.M. Grammer, J.M. Gregg, J.O. Puckette, P. Jaiswal, S.J. Mazzullo, M.J. Pranter, and R.H. Goldstein, eds., Mississippian Reservoirs of the Midcontinent: AAPG Memoir 116, doi: 10.1306/13632147M1163787.

Price, B. J., A. C. Pollack, A. P. Lamb, T. C. Peryman, and J. R. Anderson, 2020, Depositional interpretation and sequence stratigraphic control on reservoir quality and distribution in the Meremecian Sooner trend Anadarko Basin, Canadian and Kingfisher Counties (STACK) play, Anadarko Basin, Oklahoma, United States: AAPG Bulletin, **104**, no. 2, 357–386.

Read, J. F., 1995, Overview of Carbonate Platform Sequences, Cycle Stratigraphy and Reservoirs in Greenhouse and Icehouse Worlds, in Read, J.F., Kerans, C., Weber, L.J., Sarg, J.F., and Wright, F.M. (eds.), Milankovitch Sea Level Changes, Cycles, and Reservoirs on Carbonate Platforms in Greenhouse and Icehouse Worlds: SEPM Short Course 35, 1–102.

Rogers, S. M., 2001, Deposition and diagenesis of Mississippian chat reservoirs, north-central Oklahoma: AAPG Bulletin, **85**, no.1, 115–129.

Russell, B., 2014, Prestack seismic amplitude analysis: An integrated overview: Interpretation, **2**, SC19-SC36.

Russell, B., and D. Hampson, 1991, A comparison of poststack seismic inversion methods: 61st Annual International Meeting, SEG, Expanded Abstracts, 876–878.

Sams, M., and D. Carter, 2017, Stuck between a rock and a reflection: A tutorial on low-frequency models for seismic inversion: Interpretation, **5**, no. 2, B17–B27.

Serra, O., and H. T. Abbott, 1982, The contribution of logging data to sedimentary sedimentology and stratigraphy: Society of Petroleum Engineers Journal, **22**, 117–131, doi: 10.2118/9270-PA.

Sloss, L. L., 1963, Sequences in the Cratonic Interior of North America: Geological Society of America Bulletin, **74**, 93–114.

Turnini, A. M., M. J. Pranter, and K. J. Marfurt, 2019, Mississippian limestone and chert reservoirs, Tonkawa field, north-central Oklahoma, in G. M. Grammer, J. M. Gregg, J. O. Puckette, P. Jaiswal, S. J. Mazzullo, M. J. Pranter, and R. H. Goldstein, eds., Mississippian reservoirs of the midcontinent: AAPG Memoir 122, 489–511.

Watney, W. L., W. J. Guy, and A. P. Bynes, 2001, Characterization of the Mississippian chat in south-central Kansas: AAPG Bulletin, **85**, 85–113.

Wethington, N. W., and M. J. Pranter, 2018, Stratigraphic Architecture of the Mississippian Limestone through integrated electrofacies classification, Hardtner Field area, Kansas and Oklahoma, Interpretation, **6**, no. 4, T1095–T1115.

Witzke, B. J., 1990, Paleoclimatic constraints for Paleozoic paleolatitudes of Laurentia and Euramerica, W.S. McKerrow and C.R. Scotese, eds. Paleogeography and biogeography:

Geological Society (London) memoir 12, 57–73.

Xiaoxuan, A., and L. Wu, 2019, Reservoir Quality and Fractures System Assessment of Meramec and Osage Limestone by using Advanced log Analysis Method: AAPG Search and Discovery Article #90350.

Zoeppritz, K., 1919, Erdbebenwellen VIII B, Über die Reflexion und Durchgang seismischer Wellen durch Unstetigkeitsflächen: Gottinger Nachr., **1**, 66–84.

APPENDIX A: Geologic Setting

The structural history of the Anadarko Basin is complex. It can be divided into three major stages: (1) Early to Middle Cambrian rifting of Proterozoic crust, or aulacogen development; (2) Cambrian through Mississippian development of the southern Oklahoma trough from cooling and subsidence and finally; (3) Late Paleozoic tectonism forming the foreland basin through structural inversion of the core central and western part of the aulacogen (Perry, 1990).

The aulacogen phase began during the Early Cambrian when the failed arms of triple junctions extended into the North American craton during the rifting of the proto-Atlantic Ocean (Burke and Dewey, 1973; Perry, 1990). Post rifting, from Cambrian to Early Mississippian, the aulacogen began to cool and subside to form the southern Oklahoma trough, coaxial with the southern Oklahoma aulacogen (Perry, 1990). During the Mississippian, major tectonic events shaped the paleogeography of the North American craton forming the north-east to south-west trending Transcontinental Arch. The Ouchita and Wichita orogenic events were initiated during the Late Mississippian through the Early Pennsylvanian when the North America craton collided with Gondwana (Ball, 1991). This major plate collision initiated uplift of the Wichita Mountains and the Amarillo Arch. These were subsequently thrust northward over the southern Oklahoma aulacogen and trough, leading to subsidence and the formation of the Anadarko Basin (Ball, 1991).

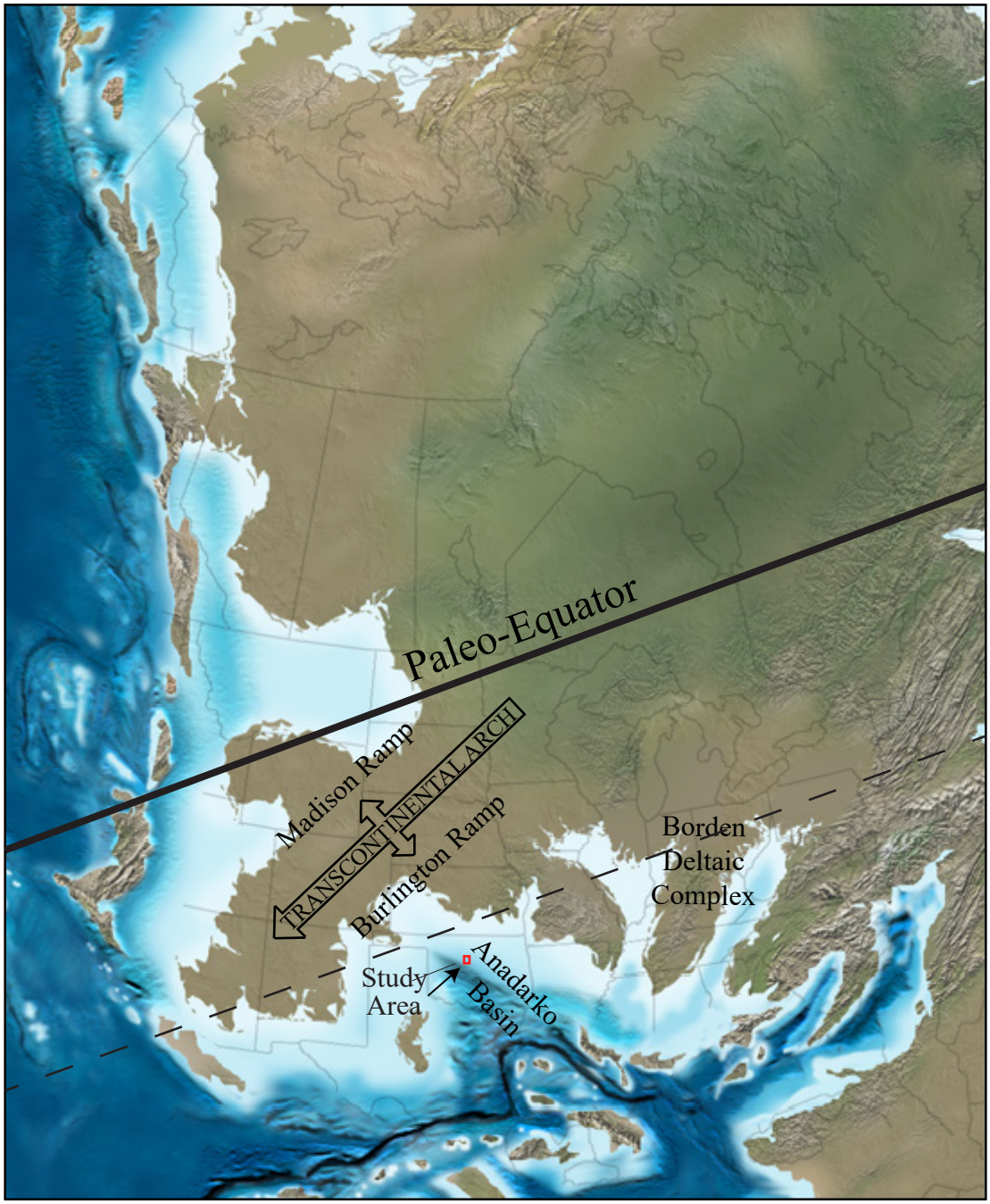

Appendix-A1: Late Mississippian paleogeographic map. The study area, outlined in red, is located in the Anadarko Basin approximately 20º southeast of the paleoequator (modified from Blakey, 2011).

APPENDIX B: Lithology and Rock-Type Definition and Classification

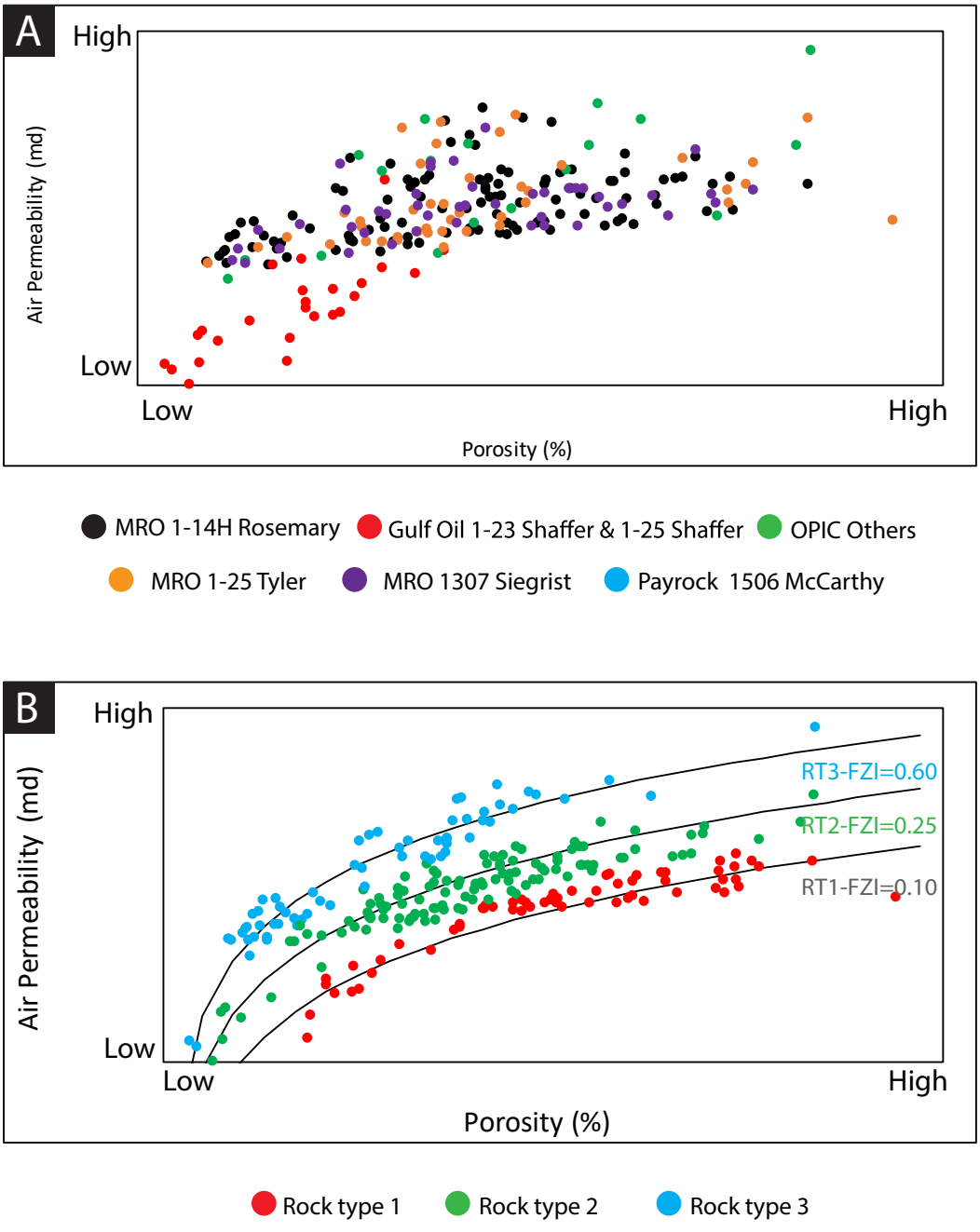

Appendix-B1: The method of deriving the petrophysical rock types. A) coss-plot of core measured air permeability (md) versus porosity. B) shows the result after the FZI equation was applied which separates the data into rock types (I. Gupta, 2018. personal communication).

APPENDIX C: Pre-stack Seismic Inversion

Both qualitative and quantitative quality control (QC) steps were applied to the results of the pre-stack inversion. These included quantitative comparisons between the frequency-filtered p-impedance, s-impedance, and density well logs with their associated seismic inversion result at the well locations, and qualitatively comparing the differences by overlying the well logs on their inversion volumes displayed by the exact same color bar (Figure 10). Additionally, the error in the inversion was analyzed by subtracting the forward modeled synthetic gathers generated from the results of the inversion from the original gathers. To reduce the error observed in the initial results, the low-frequency background model was improved by using variograms as inputs into the kriging algorithm to more accurately interpolate the high-cut frequency well-log data throughout the model according to the variograms per zone. The horizontal and vertical variograms were fit for this specific environment by using ranges determined from the lithology and rock type classification logs.

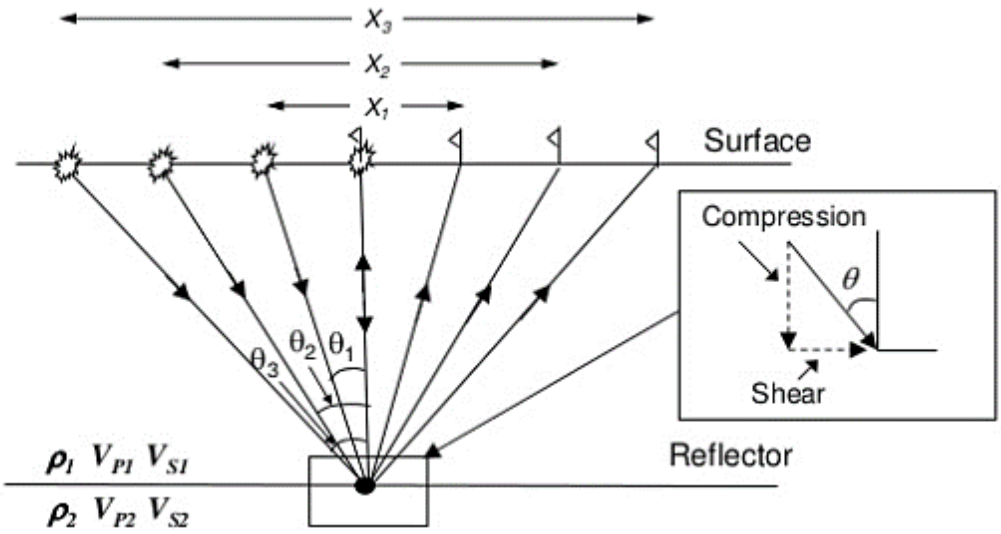

Appendix-C1: Seismic gather traces reflect from the subsurface at increasing angle of incidence ɵ related to offset X . If the angle of incidence is greater than zero, there is both a compressional and shear component (Russell, 2014).

$$(1)\ R(\theta) = \frac{1}{2}\left(\frac{\Delta V_p}{V_p} + \frac{\Delta \rho}{\rho}\right) + \left(\frac{1}{2}\frac{\Delta V_p}{V_p} - 4\frac{\Delta V_s^2}{V_p^2}\frac{\Delta V_s}{V_s} - 2\frac{\Delta V_s^2}{V_p^2}\frac{\Delta \rho}{\rho}\right)\sin^2\theta + \frac{1}{2}\frac{\Delta V_p}{V_p}\left[\tan^2\theta - \sin^2\theta\right]$$

$$(2)\ R(\theta) \approx (1 + \tan^2\theta)\frac{\Delta Z_p}{2\langle Z_p\rangle} - 8\left(\frac{\langle V_s\rangle}{\langle V_p\rangle}\right)^2 \tan^2\theta\frac{\Delta Z_s}{2\langle Z_s\rangle} + \left(-\frac{1}{2}\tan^2\theta + 2\left(\frac{\langle V_s\rangle}{\langle V_p\rangle}\right)^2 \sin^2\theta\right)\frac{\Delta\rho}{\langle\rho\rangle}$$

$$(3)\ r_p = \frac{\Delta Z_p}{Z_p} \qquad r_s = \frac{\Delta Z_s}{Z_s} \qquad r_p = \frac{\Delta\rho}{\rho}$$

Appendix-C2: The Zoeppritz equations (1919) relate the amplitude of incident p-waves to reflected and refracted p- and s- waves at a plane interface for a given angle of incidence (Russell and Hampson, 1991). Aki and Richards (2002) developed the linearized form of the Zoeppritz equations as illustrated in equation (1). This equation states that the reflectivity at angle ɵ is the weighted sum of the p-wave velocity (Vp), s-wave velocity (Vs), and density (ρ) reflectivities (Hampson et al., 2006). The components of the equation can be estimated from the pre-stack seismic gathers. Fatti et al (1994) reformulated the Aki-Richards equation to show the connection between the pre-stack and the post-stack formulations more clearly. The Fatti et al. equation (2) shows angle dependent reflectivity as a function of the Vp, Vs, and density reflectivity components (3). The angle-dependent reflectivity estimates from the Fatti et al. (1994) equation are used to invert for P-impedance, S-impedance, and density.

$$\lambda\rho = Z_p^2 - 2Z_s^2$$

$$\mu\rho = Z_s^2$$

$$\nu = \frac{\lambda\rho}{2(\lambda\rho + \mu\rho)}$$

$$E\rho = 2\mu\rho(1 + \nu)$$

ν = Poisson's Ratio
$E\rho$ = Young's Modulus
Z_p = P-impedance
Z_s = S-impedance
$\lambda\rho$ = lambda-rho
$\mu\rho$ = mu-rho
ρ = density

Appendix-C3: Geomechanical properties Poisson's Ratio and Young's Modulus are calculated using the Lame parameters of incompressibility, λ, and rigidity, μ, derived from the results of the pre-stack inversion (Goodway et al., 1997).

APPENDIX D: Velocity Modeling

$$V(Z) = V_0 + k * Z$$

V(z) = instantaneous velocity at depth Z
V_0 = initial velocity
k = well TDR
Z = depth

Appendix-D1: Linear equation used to model the instantaneous velocity variation with depth (Etris et al., 2002).

APPENDIX E: Impedance-Based Lithology and Rock-Type Relationships and Probabilities

Predicted Lithology	Actual Lithology				
	Mudstone	Argillaceous Siltstone	Arg. Calc. Siltstone	Calcareous Siltstone	Silty Limestone
Mudstone	89%	13%	5%	3%	10%
Argillaceous Siltstone	11%	46%	32%	6%	9%
Arg. Calc. Siltstone	0%	31%	47%	22%	8%
Calcareous Siltstone	0%	8%	14%	37%	18%
Silty Limestone	0%	1%	2%	31%	55%
User's Accuracy	**0.8861**	**0.4609**	**0.4684**	**0.3742**	**0.5494**

Overall Accuracy: 55%

Appendix-E1: Confusion matrices displaying the accuracies for the impedance-based lithology prediction for all lithologies.

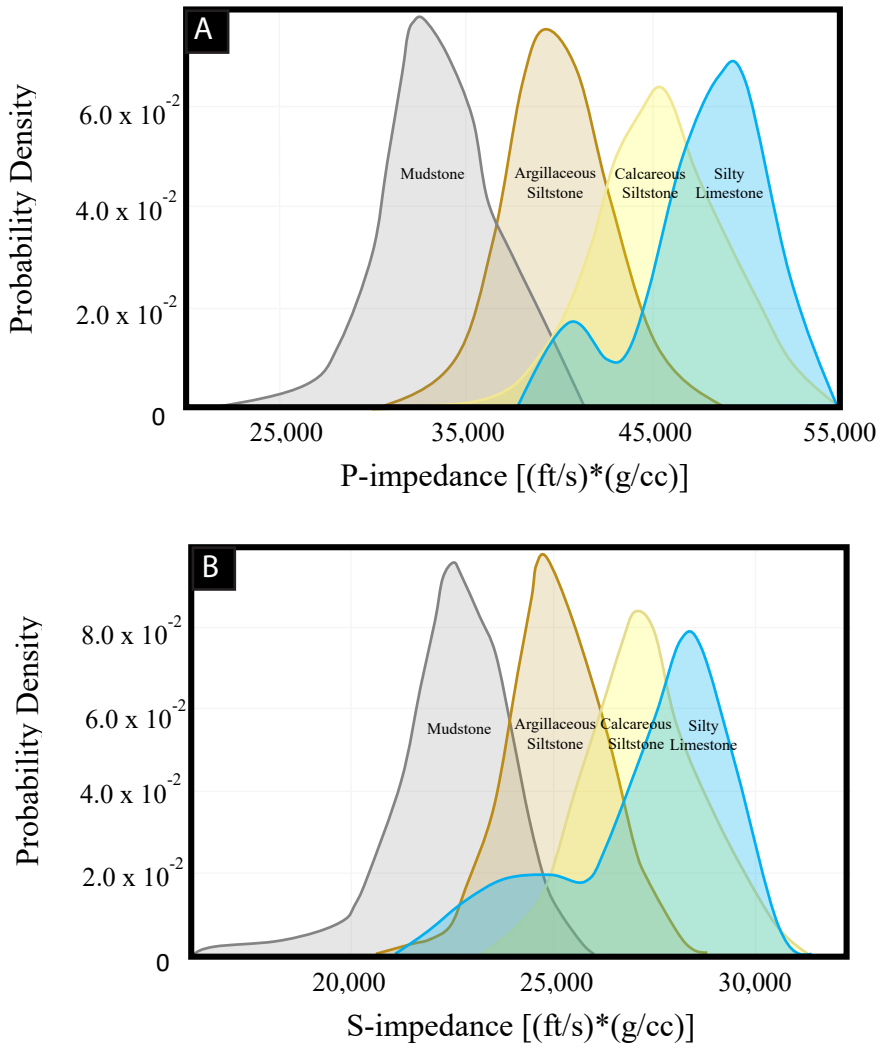

Appendix-E2: A) shows the probability of predicting each lithology according to its P-impedance response. B) The probability of predicting each lithology according to its S-impedance response.

APPENDIX F: Spatial Distribution of Reservoir Properties

Variogram Parameters for Lithology Modeling (Mudstone)

Zone	Major (ft)	Minor (ft)	Vertical (ft)	Azimuth (degrees from N)
Meramec 7	1,079	580	2.544	-10
Meramec 6	2,334	777	6.608	-10
Meramec 5	3,380	1,546	6.61	-10
Meramec 4	1,369	757	2.745	-10
Meramec 3	2,390	1,618	2.733	-10
Meramec 2	1,723	1,610	2.315	-10
Meramec 1	1,779	1,690	4.378	-10

Variogram Parameters for Lithology Modeling (Argillaceous Siltstone)

Zone	Major (ft)	Minor (ft)	Vertical (ft)	Azimuth (degrees from N)
Meramec 7	1,014	592	3.141	5
Meramec 6	1,843	733	1.617	5
Meramec 5	1,763	1,417	2.354	5
Meramec 4	1,562	1,212	3.064	5
Meramec 3	2,213	1,747	2.403	5
Meramec 2	1,698	1,532	3.347	5
Meramec 1	2,141	1,843	2.79	5

Variogram Parameters for Lithology Modeling (Argillaceous-Calcareous Siltstone)

Zone	Major (ft)	Minor (ft)	Vertical (ft)	Azimuth (degrees from N)
Meramec 7	1,014	592	3.141	5
Meramec 6	1,843	733	1.617	5
Meramec 5	1,763	1,417	2.354	5
Meramec 4	1,562	1,212	3.064	5
Meramec 3	2,213	1,747	2.403	5
Meramec 2	1,698	1,532	3.347	5
Meramec 1	2,141	1,843	2.79	5

Appendix-F1: Variogram ranges and azimuth for the P50 lithology model separated by zone. Horizontal ranges were estimated from the lithology classification log. The vertical ranges were estimated through variography for each zone by lithology. The azimuth was estimated from the lithology probability volumes.

Variogram Parameters for Lithology Modeling (Calcareous Siltstone)

Zone	Major (ft)	Minor (ft)	Vertical (ft)	Azimuth (degrees from N)
Meramec 7	1,980	1,075	4.597	-5
Meramec 6	1,948	1,051	2.823	-5
Meramec 5	2,407	1,115	3.378	-5
Meramec 4	1,948	1,087	3.49	-5
Meramec 3	1,248	1,200	3.064	-5
Meramec 2	1,200	1,135	4.615	-5
Meramec 1	1,288	1,167	3.497	-5

Variogram Parameters for Lithology Modeling (Silty Limestone)

Zone	Major (ft)	Minor (ft)	Vertical (ft)	Azimuth (degrees from N)
Meramec 7	3,500	1,750	4.551	-5
Meramec 6	3,500	1,750	4.551	-5
Meramec 5	3,500	1,750	4.551	-5
Meramec 4	3,500	1,750	4.551	-5
Meramec 3	1,988	1,892	1.976	-5
Meramec 2	2,390	1,698	3.313	-5
Meramec 1	2,471	2,101	4.378	-5

Appendix-F1 cont'd: Variogram ranges and azimuth for the P50 lithology model separated by zone. Horizontal ranges were estimated from the lithology classification log. The vertical ranges were estimated through variography for each zone by lithology. The azimuth was estimated from the lithology probability volumes.

Variogram Parameters for Rock Type Modeling (Rock Type 1)

Zone	Major (ft)	Minor (ft)	Vertical (ft)	Azimuth (degrees from N)
Meramec 7	2,044	1,682	4.281	0
Meramec 6	1,980	1,739	3.064	0
Meramec 5	2,865	2,447	2.374	0
Meramec 4	3,879	3,622	3.833	0
Meramec 3	3,235	2,833	3.326	0
Meramec 2	3,384	2,696	3.161	0
Meramec 1	4,491	4,072	3.708	0

Variogram Parameters for Rock Type Modeling (Rock Type 2)

Zone	Major (ft)	Minor (ft)	Vertical (ft)	Azimuth (degrees from N)
Meramec 7	1,795	1,674	2.025	0
Meramec 6	2,044	1,819	3.253	0
Meramec 5	1,377	1,248	2.616	0
Meramec 4	1,377	1,248	3.221	0
Meramec 3	1,621	1,481	2.496	0
Meramec 2	1,706	1,578	3.504	0
Meramec 1	1,674	1,594	4.318	0

Variogram Parameters for Rock Type Modeling (Rock Type 3)

Zone	Major (ft)	Minor (ft)	Vertical (ft)	Azimuth (degrees from N)
Meramec 7	2,077	1,417	7.608	-2
Meramec 6	1,996	1,594	3.442	-2
Meramec 5	1,867	1,578	2.943	-2
Meramec 4	1,731	1,578	4.671	-2
Meramec 3	2,238	2,093	2.781	-2
Meramec 2	2,293	2,165	4.132	-2
Meramec 1	3,799	3,412	4.318	-2

Appendix-F2: Variogram ranges and azimuth for the P50 rock-type model separated by zone. Horizontal ranges were estimated from the rock-type classification log. The vertical ranges were estimated through variography for each zone by lithology. The azimuth was estimated from the lithology probability volumes.

Variogram Parameters for Porosity Modeling (Mudstone)

Zone	Major (ft)	Minor (ft)	Vertical (ft)	Azimuth (degrees from N)
Meramec 7	2,000	1,000	2.292	-10
Meramec 6	2,000	1,000	3.442	-10
Meramec 5	2,000	1,000	3.89	-10
Meramec 4	2,000	1,000	4.105	-10
Meramec 3	2,000	1,000	3.064	-10
Meramec 2	2,000	1,000	3.071	-10
Meramec 1	2,000	1,000	2	-10

Variogram Parameters for Porosity Modeling (Argillaceous Siltstone)

Zone	Major (ft)	Minor (ft)	Vertical (ft)	Azimuth (degrees from N)
Meramec 7	2,000	1,000	2.158	5
Meramec 6	2,000	1,000	4.807	5
Meramec 5	2,000	1,000	4.079	5
Meramec 4	2,000	1,000	2.306	5
Meramec 3	2,000	1,000	3.442	5
Meramec 2	2,000	1,000	3.632	5
Meramec 1	2,000	1,000	3.821	5

Variogram Parameters for Porosity Modeling (Argillaceous-Calcareous Siltstone)

Zone	Major (ft)	Minor (ft)	Vertical (ft)	Azimuth (degrees from N)
Meramec 7	2,000	1,000	3.89	5
Meramec 6	2,000	1,000	4.01	5
Meramec 5	2,000	1,000	3.768	5
Meramec 4	2,000	1,000	3.544	5
Meramec 3	2,000	1,000	3.821	5
Meramec 2	2,000	1,000	3.632	5
Meramec 1	2,000	1,000	3.855	5

Appendix-F3: Variogram ranges and azimuth for the P50 total porosity model separated by zone. Horizontal ranges were decreased from the lithology model. The vertical ranges were estimated through variography for each zone by lithology. The azimuth was estimated from the lithology probability volumes.

Variogram Parameters for Porosity Modeling (Calcareous Siltstone)

Zone	Major (ft)	Minor (ft)	Vertical (ft)	Azimuth (degrees from N)
Meramec 7	2,000	1,000	3.788	-5
Meramec 6	2,000	1,000	3.935	-5
Meramec 5	2,000	1,000	4.112	-5
Meramec 4	2,000	1,000	4.09	-5
Meramec 3	2,000	1,000	4.476	-5
Meramec 2	2,000	1,000	4.544	-5
Meramec 1	2,000	1,000	4.798	-5

Variogram Parameters for Porosity Modeling (Silty Limestone)

Zone	Major (ft)	Minor (ft)	Vertical (ft)	Azimuth (degrees from N)
Meramec 7	2,000	1,000	2.306	-5
Meramec 6	2,000	1,000	3.923	-5
Meramec 5	2,000	1,000	3.912	-5
Meramec 4	2,000	1,000	4.079	-5
Meramec 3	2,000	1,000	2.164	-5
Meramec 2	2,000	1,000	3.253	-5
Meramec 1	2,000	1,000	3.632	-5

Appendix-F3 cont'd: Variogram ranges and azimuth for the P50 total porosity model separated by zone. Horizontal ranges were decreased from the lithology model. The vertical ranges were estimated through variography for each zone by lithology. The azimuth was estimated from the lithology probability volumes.

Variogram Parameters for Porosity Modeling (Rock Type 1)

Zone	Major (ft)	Minor (ft)	Vertical (ft)	Azimuth (degrees from N)
Meramec 7	2,000	1,000	3.594	0
Meramec 6	2,000	1,000	2.874	0
Meramec 5	2,000	1,000	2.393	0
Meramec 4	2,000	1,000	2.496	0
Meramec 3	2,000	1,000	3.458	0
Meramec 2	2,000	1,000	3.579	0
Meramec 1	2,000	1,000	3.253	0

Variogram Parameters for Porosity Modeling (Rock Type 2)

Zone	Major (ft)	Minor (ft)	Vertical (ft)	Azimuth (degrees from N)
Meramec 7	2,000	1,000	2.685	0
Meramec 6	2,000	1,000	3.442	0
Meramec 5	2,000	1,000	3.064	0
Meramec 4	2,000	1,000	2.117	0
Meramec 3	2,000	1,000	2.837	0
Meramec 2	2,000	1,000	3.442	0
Meramec 1	2,000	1,000	2.874	0

Variogram Parameters for Porosity Modeling (Rock Type 3)

Zone	Major (ft)	Minor (ft)	Vertical (ft)	Azimuth (degrees from N)
Meramec 7	2,000	1,000	3.632	-2
Meramec 6	2,000	1,000	3.253	-2
Meramec 5	2,000	1,000	4.37	-2
Meramec 4	2,000	1,000	2.893	-2
Meramec 3	2,000	1,000	3.821	-2
Meramec 2	2,000	1,000	4.063	-2
Meramec 1	2,000	1,000	3.253	-2

Appendix-F4: Variogram ranges and azimuth for the P50 total porosity model separated by zone. Horizontal ranges were decreased from the rock-type model. The vertical ranges were estimated through variography for each zone by rock type. The azimuth was estimated from the rock-type probability volumes.

Variogram Parameters for Water Saturation Modeling (Mudstone)

Zone	Major (ft)	Minor (ft)	Vertical (ft)	Azimuth (degrees from N)
Meramec 7	1,079	580	2.544	-10
Meramec 6	2,334	777	6.608	-10
Meramec 5	3,380	1,546	6.61	-10
Meramec 4	1,369	757	2.745	-10
Meramec 3	2,390	1,618	2.733	-10
Meramec 2	1,723	1,610	2.315	-10
Meramec 1	1,779	1,690	4.378	-10

Variogram Parameters for Water Saturation Modeling (Argillaceous Siltstone)

Zone	Major (ft)	Minor (ft)	Vertical (ft)	Azimuth (degrees from N)
Meramec 7	1,014	592	3.141	5
Meramec 6	1,843	733	1.617	5
Meramec 5	1,763	1,417	2.354	5
Meramec 4	1,562	1,212	3.064	5
Meramec 3	2,213	1,747	2.403	5
Meramec 2	1,698	1,532	3.347	5
Meramec 1	2,141	1,843	2.79	5

Variogram Parameters for Water Saturation Modeling (Argillaceous-Calcareous Siltstone)

Zone	Major (ft)	Minor (ft)	Vertical (ft)	Azimuth (degrees from N)
Meramec 7	1,014	592	3.141	5
Meramec 6	1,843	733	1.617	5
Meramec 5	1,763	1,417	2.354	5
Meramec 4	1,562	1,212	3.064	5
Meramec 3	2,213	1,747	2.403	5
Meramec 2	1,698	1,532	3.347	5
Meramec 1	2,141	1,843	2.79	5

Appendix-F5: Variogram ranges and azimuth for the P50 water saturation model separated by zone. Horizontal ranges were decreased from the lithology model. The vertical ranges were estimated through variography for each zone by lithology. The azimuth was estimated from the lithology probability volumes.

Variogram Parameters for Lithology Modeling (Calcareous Siltstone)				
Zone	Major (ft)	Minor (ft)	Vertical (ft)	Azimuth (degrees from N)
Meramec 7	1,980	1,075	4.597	-5
Meramec 6	1,948	1,051	2.823	-5
Meramec 5	2,407	1,115	3.378	-5
Meramec 4	1,948	1,087	3.49	-5
Meramec 3	1,248	1,200	3.064	-5
Meramec 2	1,200	1,135	4.615	-5
Meramec 1	1,288	1,167	3.497	-5

Variogram Parameters for Lithology Modeling (Silty Limestone)				
Zone	Major (ft)	Minor (ft)	Vertical (ft)	Azimuth (degrees from N)
Meramec 7	3,500	1,750	4.551	-5
Meramec 6	3,500	1,750	4.551	-5
Meramec 5	3,500	1,750	4.551	-5
Meramec 4	3,500	1,750	4.551	-5
Meramec 3	1,988	1,892	1.976	-5
Meramec 2	2,390	1,698	3.313	-5
Meramec 1	2,471	2,101	4.378	-5

Appendix-F5 cont'd: Variogram ranges and azimuth for the P50 water saturation model separated by zone. Horizontal ranges were decreased from the lithology model. The vertical ranges were estimated through variography for each zone by lithology. The azimuth was estimated from the lithology probability volumes.

Variogram Parameters for Water Saturation Modeling (Rock Type 1)

Zone	Major (ft)	Minor (ft)	Vertical (ft)	Azimuth (degrees from N)
Meramec 7	2,000	1,000	3.594	0
Meramec 6	2,000	1,000	2.874	0
Meramec 5	2,000	1,000	3.393	0
Meramec 4	2,000	1,000	2.496	0
Meramec 3	2,000	1,000	3.458	0
Meramec 2	2,000	1,000	3.579	0
Meramec 1	2,000	1,000	3.253	0

Variogram Parameters for Water Saturation Modeling (Rock Type 2)

Zone	Major (ft)	Minor (ft)	Vertical (ft)	Azimuth (degrees from N)
Meramec 7	2,000	1,000	2.685	0
Meramec 6	2,000	1,000	3.442	0
Meramec 5	2,000	1,000	3.064	0
Meramec 4	2,000	1,000	2.117	0
Meramec 3	2,000	1,000	2.837	0
Meramec 2	2,000	1,000	3.442	0
Meramec 1	2,000	1,000	2.874	0

Variogram Parameters for Water Saturation Modeling (Rock Type 3)

Zone	Major (ft)	Minor (ft)	Vertical (ft)	Azimuth (degrees from N)
Meramec 7	2,000	1,000	3.632	-2
Meramec 6	2,000	1,000	3.253	-2
Meramec 5	2,000	1,000	4.37	-2
Meramec 4	2,000	1,000	2.893	-2
Meramec 3	2,000	1,000	3.821	-2
Meramec 2	2,000	1,000	4.063	-2
Meramec 1	2,000	1,000	3.253	-2

Appendix-F6: Variogram ranges and azimuth for the P50 water saturation model separated by zone. Horizontal ranges were decreased from the rock-type model. The vertical ranges were estimated through variography for each zone by rock type. The azimuth was estimated from the rock-type probability volumes.

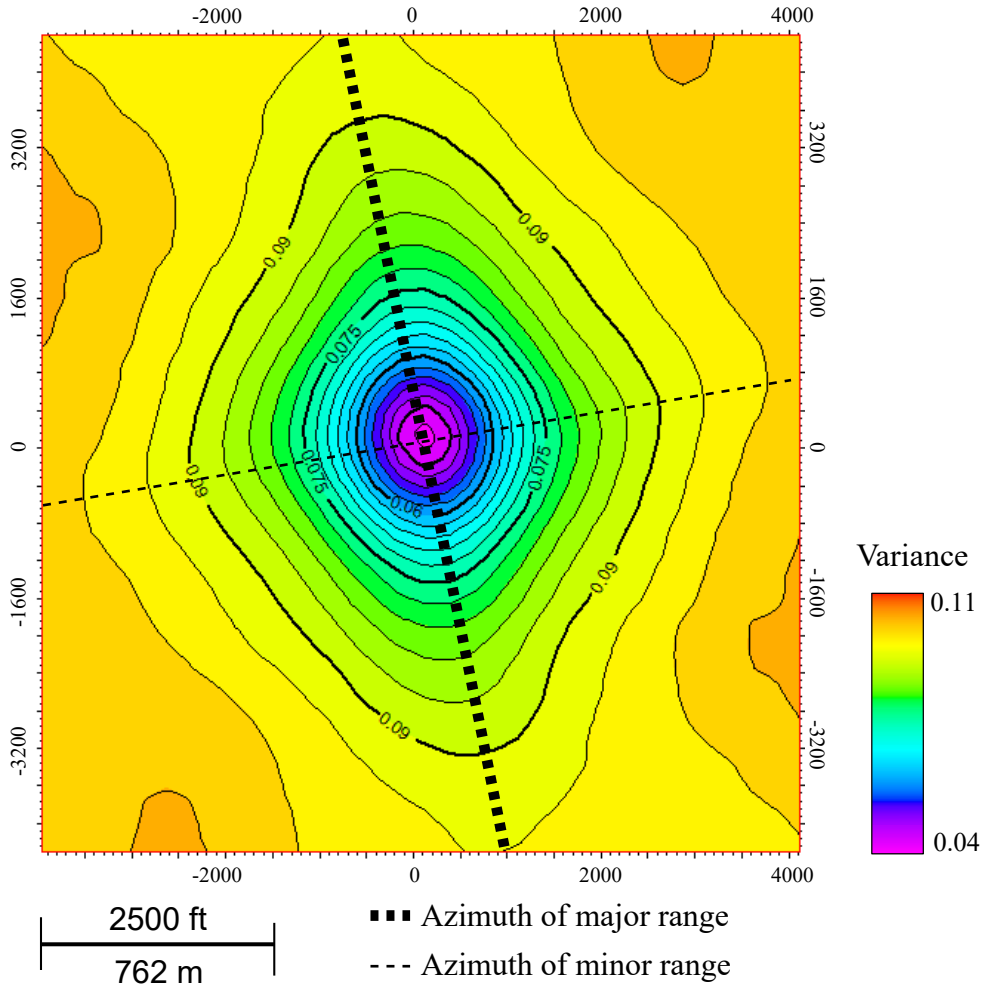

Appendix-F7: Variogram map for mudstone generated from the mudstone probability volume shows the greatest lateral continuity for this lithology to be approximately -10º from North. This indicates the azimuth of the major range. The minor direction is perpendicular to the major at approximately 80º from North. This is where the greatest amount of lateral heterogeneity is observed.

APPENDIX G: Volumetrics

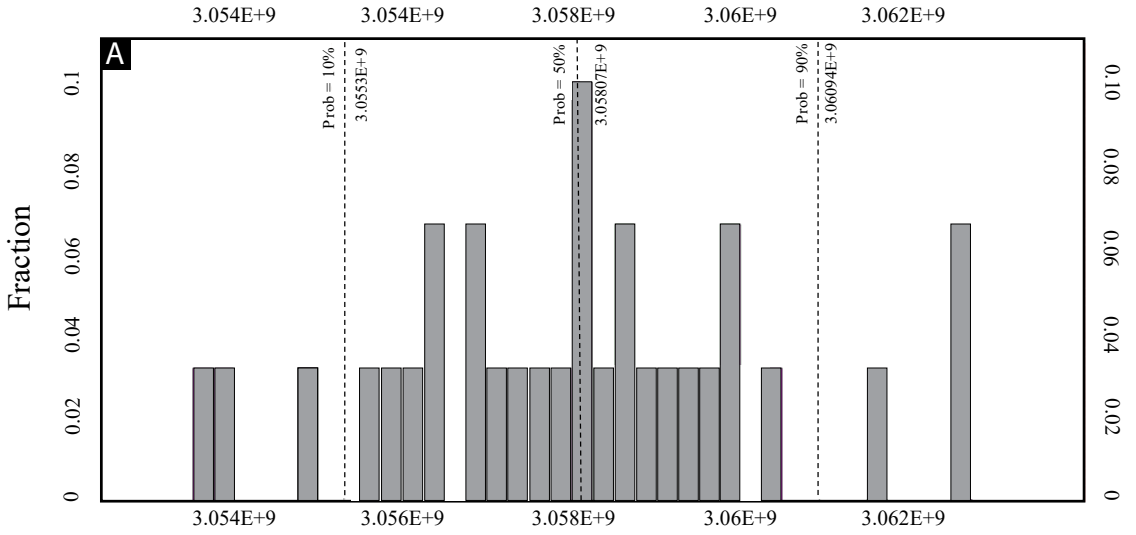

Pore Volume (RB) from Lithology Model

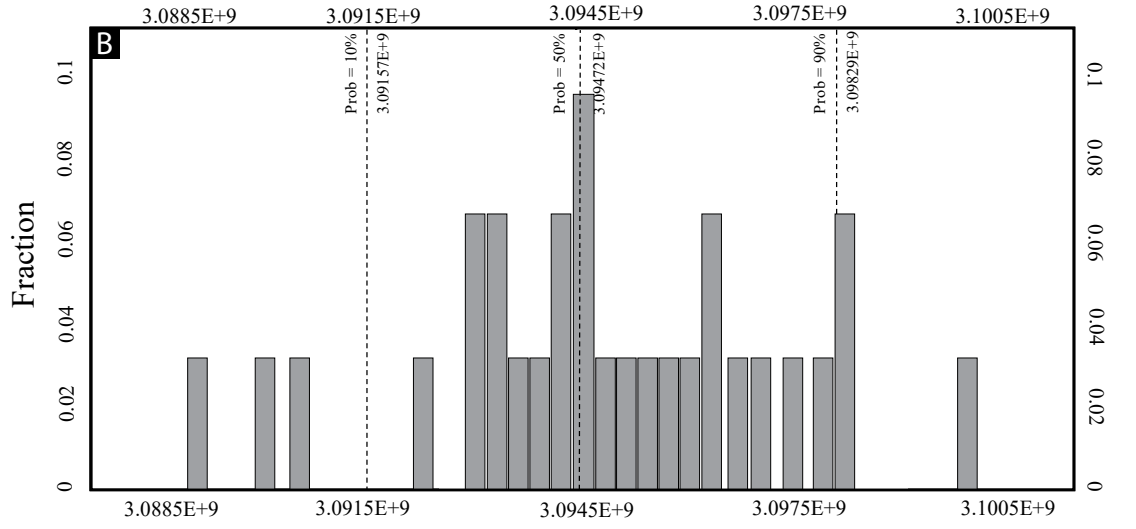

Pore Volume (RB) from Rock Type Model

Appendix-G1: Histograms of the pore volume showing results for 30 model realizations for (A) the lithology model and its associated petrophysical properties, and (B) the rock-type model and its associated petrophysical properties. The histograms indicate the P10, P50 and P90 values of pore volume.

Lithology Model			
P10 Volumetric Calculations			
Zone	Bulk Volume ($*10^6$ ft^3)	Pore Volume ($*10^6$ RB)	Hydrocarbon Pore Volume ($*10^6$ RB)
Meramec G	12,882	175	112
Meramec F	15,175	178	125
Meramec E	51,464	348	215
Meramec D	88,103	903	648
Meramec B	70,338	665	462
Meramec B10	62,653	427	271
Meramec A	63,900	357	233
Total	364,515	3,053	2,066
P50 Volumetric Calculations			
Zone	Bulk Volume ($*10^6$ ft^3)	Pore Volume ($*10^6$ RB)	Hydrocarbon Pore Volume ($*10^6$ RB)
Meramec G	12,882	175	112
Meramec F	15,175	178	125
Meramec E	51,464	350	215
Meramec D	88,103	904	649
Meramec B	70,338	665	462
Meramec B10	62,653	427	271
Meramec A	63,900	359	233
Total	364,515	3,058	2,067
P90 Volumetric Calculations			
Zone	Bulk Volume ($*10^6$ ft^3)	Pore Volume ($*10^6$ RB)	Hydrocarbon Pore Volume ($*10^6$ RB)
Meramec G	12,882	175	112
Meramec F	15,175	178	125
Meramec E	51,464	349	215
Meramec D	88,103	904	651
Meramec B	70,338	667	462
Meramec B10	62,653	428	272
Meramec A	63,900	358	232
Total	364,515	3,059	2,069

Appendix-G2: Results from the volumetric analysis over the township using the lithology model and the associated petrophysical models. P10, P50, and P90 volumetric calculations are indicated.

Rock Type Model			
P10 Volumetric Calculations			
Zone	Bulk Volume ($*10^6$ ^{3})	Pore Volume ($*10^6$ RB)	Hydrocarbon Pore Volume ($*10^6$ RB)
Meramec G	12,882	200	133
Meramec F	15,175	178	126
Meramec E	51,464	350	216
Meramec D	88,103	903	649
Meramec B	70,338	664	468
Meramec B10	62,653	426	277
Meramec A	63,900	369	245
Total	364,515	3,090	2,114
P50 Volumetric Calculations			
Zone	Bulk Volume ($*10^6$ ^{3})	Pore Volume ($*10^6$ RB)	Hydrocarbon Pore Volume ($*10^6$ RB)
Meramec G	12,882	199	132
Meramec F	15,175	179	127
Meramec E	51,464	351	216
Meramec D	88,103	903	649
Meramec B	70,338	664	468
Meramec B10	62,653	429	279
Meramec A	63,900	369	245
Total	364,515	3,094	2,116
P90 Volumetric Calculations			
Zone	Bulk Volume ($*10^6$ ^{3})	Pore Volume ($*10^6$ RB)	Hydrocarbon Pore Volume ($*10^6$ RB)
Meramec G	12,882	199	133
Meramec F	15,175	179	127
Meramec E	51,464	354	217
Meramec D	88,103	904	650
Meramec B	70,338	665	469
Meramec B10	62,653	428	279
Meramec A	63,900	370	245
Total	364,515	3,099	2,120

Appendix-G3: Results from the volumetric analysis over the township using the rock type model and the associated petrophysical models. P10, P50, and P90 volumetric calculations are indicated.

APPENDIX H: Production Analysis

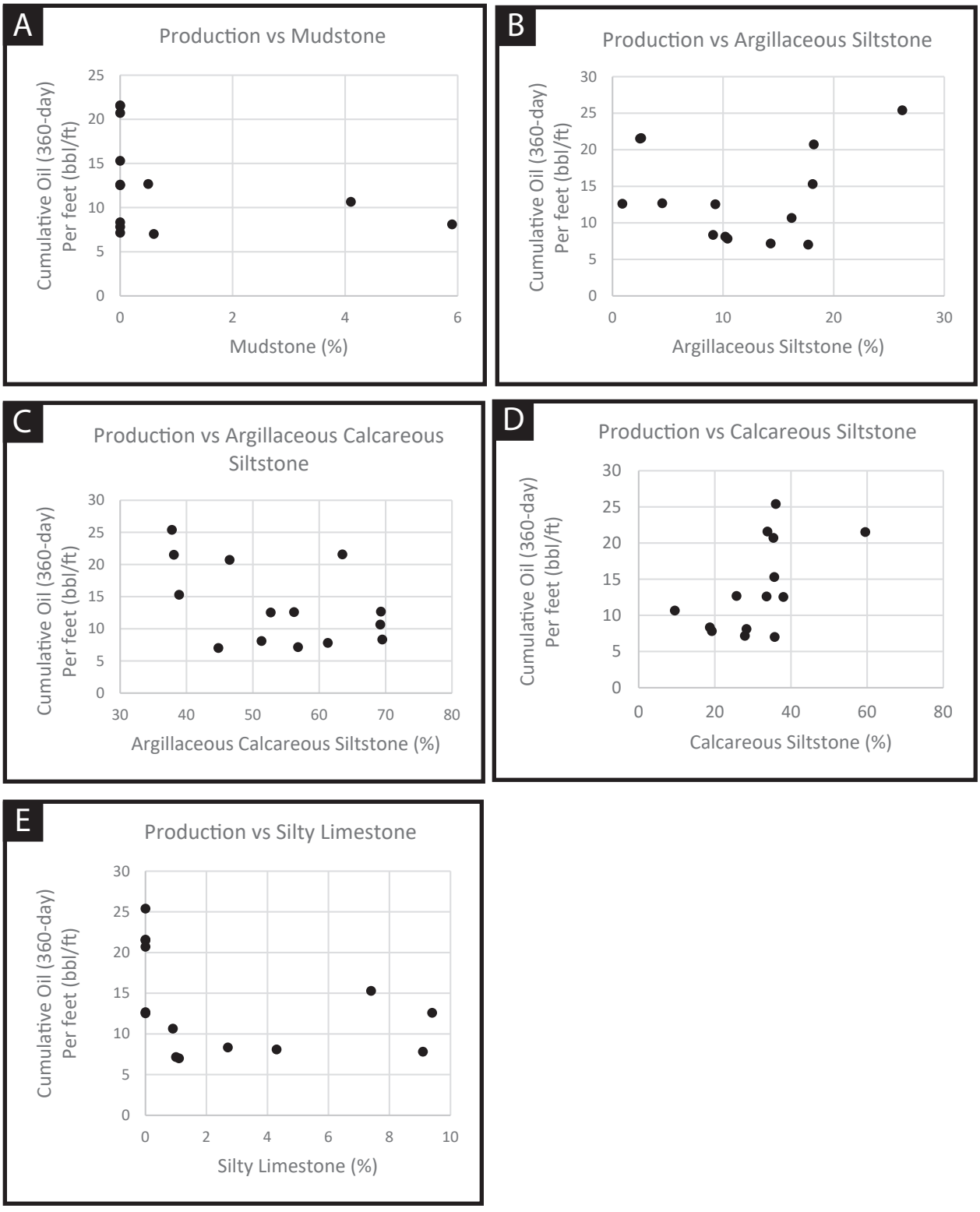

Appendix-H1: 180-day cumulative oil production are compared to the percentage of each lithology along the lateral of 13 producing wells. The results show no clear correlations.